

UNIVERSITY OF SOUTHAMPTON  
FACULTY OF PHYSICAL SCIENCES AND ENGINEERING  
Department of Physics & Astronomy

# **Disc Winds Matter: Modelling Accretion and Outflow on All Scales**

by  
James Matthews

A thesis submitted for the degree of Doctor of Philosophy

May 2016



*“Here, on the edge of what we know, in contact with the ocean of the unknown, shines the mystery and the beauty of the world.*

*And it’s breathtaking.”*

Seven Brief Lessons on Physics, Carlo Rovelli

*“Good enough for government work.”*

Christian Knigge



UNIVERSITY OF SOUTHAMPTON

## ABSTRACT

FACULTY OF PHYSICAL SCIENCES AND ENGINEERING

Department of Physics & Astronomy

Doctor of Philosophy

### **DISC WINDS MATTER: MODELLING ACCRETION AND OUTFLOW ON ALL SCALES**

by James Matthews

Outflows are ubiquitous in accreting systems across 10 orders of magnitude in mass, and there is good evidence that mass-loaded winds are launched from the accretion discs of quasars and cataclysmic variables (CVs). Perhaps the most spectacular evidence for accretion disc winds is the blue-shifted, broad absorption lines (BALs) in UV resonance lines, seen in CVs and the BAL quasars. As well as imprinting absorption features, disc winds may affect the line and continuum emission from accreting objects. They thus offer a natural way to *unify* much of the phenomenology of CVs and active galactic nuclei (AGN).

In this thesis, I use a state-of-the-art Monte Carlo radiative transfer (MCRT) code, PYTHON, to conduct a series of simulations designed to test simple biconical disc wind models. I outline the MCRT techniques used, before describing a series of code validation exercises. Having tested my methods thoroughly, I explore whether the winds that are responsible for the UV BALs in high-state CVs could also have an effect on the optical spectrum. I find that the wind produces strong emission in the Balmer series, He II 4686 Å and a series of He I lines. The model shows the observed trends with inclination and in some cases produces sufficient recombination continuum emission to fill in the Balmer photoabsorption edge intrinsic to disc atmospheres. The results suggest that disc winds could have a significant impact on the optical spectra of high-state CVs.

The next step was to apply the techniques to quasar winds in a test of disc wind unification models. In previous efforts, the outflow tended to become ‘over-ionized’, and BAL features were only present if the X-ray luminosity was limited to around  $10^{43}$  erg s $^{-1}$ . The outflow also failed to produce significant line emission. Motivated by these problems, I introduce a simple treatment of clumping and find that it allows BAL features to form in the rest-frame UV at more realistic X-ray luminosities. The fiducial model shows good agreement with AGN X-ray properties and the wind produces strong line emission. Despite these successes, the model cannot reproduce all emission lines seen in quasar spectra with the correct equivalent width (EW) ratios, and I find the emission line EWs have a strong dependence on inclination.

Informed by the quasar wind modelling, I examine the emission line EW distributions of quasars in the context of geometric unification. I find that the observed distributions are not consistent with a model in which an equatorial BAL outflow rises from a foreshortened accretion disc. I discuss this finding in the context of other observational orientation indicators. Finally, I summarise my findings and suggest avenues for future work. Overall, the work presented here suggests that *disc winds matter*. They not only act as a spectral ‘filter’ for the underlying accretion continuum, but may actually dominate the emergent spectrum from accreting objects. As a result, unveiling their driving mechanisms, mass-loss rates and ionization structure is an important goal for the astronomical community.



# Contents

<b>Abstract</b>	<b>iv</b>
<b>List of Figures</b>	<b>ix</b>
<b>List of Tables</b>	<b>xi</b>
<b>Declaration of Authorship</b>	<b>xiii</b>
<b>Acknowledgements</b>	<b>xv</b>
<b>Abbreviations</b>	<b>xvii</b>
<b>Physical Constants</b>	<b>xix</b>
<b>1 Introduction</b>	<b>1</b>
1.1 The Physics of Accretion . . . . .	3
1.1.1 Spherical Accretion and The Eddington Limit . . . . .	4
1.1.2 Accretion Discs . . . . .	5
1.1.2.1 Steady-state Accretion Discs: the $\alpha$ -prescription . . . . .	6
1.1.3 Boundary Layers, Black Hole Spin and the ISCO . . . . .	8
1.1.4 The Emergent Spectrum . . . . .	11
1.2 Accreting Compact Binaries . . . . .	12
1.2.1 Roche Lobe-Overflow . . . . .	14
1.2.2 Cataclysmic Variables . . . . .	15
1.2.2.1 Dwarf Novae and the Disc-instability Model . . . . .	16
1.2.2.2 Nova-like Variables . . . . .	16
1.2.3 Low Mass X-ray Binaries . . . . .	17
1.3 Quasars and Active Galactic Nuclei . . . . .	20
1.3.1 AGN Unification and the Dusty Torus . . . . .	23
1.3.2 X-ray Properties of AGN . . . . .	25
1.3.2.1 The Soft X-ray Excess . . . . .	26
1.3.3 The Broad Line Region: Connection to Winds and Unification . . . . .	27
1.4 The Current Understanding of the Disc Continuum . . . . .	27
1.4.1 The Spectral Shape of CV Discs . . . . .	28
1.4.2 The Big Blue Bump in AGN . . . . .	29
1.4.2.1 The Accretion Disc Size Problem . . . . .	29
1.4.2.2 Fitting AGN Spectra and the 1000 Å Break . . . . .	29
1.5 The Universality of Accretion . . . . .	30
1.5.1 The RMS-flux relation . . . . .	30
1.5.2 Accretion states and disc-jet coupling . . . . .	31
1.5.3 A Global Picture . . . . .	32

<b>2 Quasar Emission Lines as Probes of Orientation and Unification</b>	<b>33</b>
2.1 Introduction . . . . .	33
2.2 Data Sample . . . . .	35
2.3 The Angular Distribution of Emission from an Accretion Disc . . . . .	39
2.3.1 Standard Thin Disc Models . . . . .	39
2.3.2 Including GR and Opacity Effects . . . . .	40
2.4 Predicted EW Distributions Compared to Observations . . . . .	40
2.4.1 Fitting the Quasar Distribution . . . . .	40
2.4.2 Comparing non-BAL and LoBAL Distributions: Sample A . . . . .	44
2.5 Discussion . . . . .	47
2.5.1 Eigenvector 1 . . . . .	48
2.5.2 Polarisation . . . . .	49
2.5.3 The Effect of Obscuration . . . . .	53
2.5.4 Line Anisotropy . . . . .	54
2.6 Conclusions . . . . .	55
<b>Bibliography</b>	<b>59</b>

# List of Figures

1.1	The temperature profile of an accretion disc for three different classes of compact object. . . . .	8
1.2	Angular velocity as a function of radius in an accretion disc around a rotating compact object. . . . .	9
1.3	The radius of the ISCO, $R_{ISCO}$ , and the horizon, $R_H$ , is as a function of the BH spin parameter, $a_*$ . . . . .	10
1.4	Accretion disc SEDs for three different compact objects. . . . .	11
1.5	A comparison between an accretion disc spectrum computed with black-body and stellar atmosphere spectra. . . . .	12
1.6	Artists impression of an LMXB and CV. . . . .	13
1.7	The Roche potential in a binary system . . . . .	14
1.8	A year in the life of SS Cyg. . . . .	17
1.9	Spectra of SS Cyg during an outburst cycle . . . . .	18
1.10	Optical spectra of three nova-like variables. . . . .	19
1.11	UV spectrum of RW Tri in and out of eclipse. . . . .	20
1.12	Template spectra, from the AGN atlas, for four common types of AGN. .	22
1.13	A unified scheme for AGN. . . . .	24
1.14	Broadband SEDs for different AGN SEDs . . . . .	25
1.15	Occam's quasar . . . . .	28
1.16	Hardness-intensity diagrams for three types of accreting objects. . . . .	32
2.1	BH mass and Eddington fraction measurements for samples A and B. .	36
2.2	Histograms of equivalent widths for three emission lines from the two different samples. . . . .	37
2.3	Angular variation of continuum luminosity from AGNSPEC and classical thin disc models. . . . .	41
2.4	Theoretical EW distributions from the numerical experiment described in section 2.4.1. . . . .	43
2.5	The EW[O III] distribution of quasars in the R11 sample and the best fit model. . . . .	45
2.6	$\chi^2/dof$ as a function of maximum angle. . . . .	46
2.7	The geometry of the toy model used to carry out the Monte Carlo simulations. . . . .	46
2.8	Heat map showing the results of the MC simulation described in section 2.4.2. . . . .	48
2.9	Eigenvector 1 for BAL and non-BAL quasars. . . . .	50
2.10	LoBAL fraction compared to global LoBAL fraction in Eigenvector 1 space.	51
2.11	FWHM BLAH. . . . .	51

2.12 Histograms of polarisation percentages for BAL quasars from Schmidt et al. (1999) together with the Marin et al. (2014) AGN sample. . . . .	52
2.13 Cumulative distribution functions of the histograms shown in Fig. 2.12 for BAL quasars from Schmidt et al. (1999) together with the Marin et al. (2014) AGN sample. The colour-coding and $x$ -axis scale are the same as Fig. 2.12. The translucent vertical lines mark the median value in each sample. . . . .	52

# List of Tables

1.1 Approximate values of compactness and accretion efficiency for four different compact objects. . . . .	4
--	---



# Declaration of Authorship

I, James Matthews, declare that this thesis titled, ‘Disc Winds Matter: Modelling Accretion and Outflow on All Scales’ and the work presented in it are my own. I confirm that:

- This work was done wholly or mainly while in candidature for a research degree at this University.
- Where any part of this thesis has previously been submitted for a degree or any other qualification at this University or any other institution, this has been clearly stated.
- Where I have consulted the published work of others, this is always clearly attributed.
- Where I have quoted from the work of others, the source is always given. With the exception of such quotations, this thesis is entirely my own work.
- I have acknowledged all main sources of help.
- Where the thesis is based on work done by myself jointly with others, I have made clear exactly what was done by others and what I have contributed myself.

The first two chapters of this thesis provide a general introduction to the field, and thus are based on the relevant literature. Where a figure is not produced by me, I have acknowledged this clearly with a credit to the relevant publication. Chapter 3 contains a description of the methods used. This is partly a description of the radiative transfer code PYTHON, which was originally developed by Knox Long and Christian Knigge ([Long & Knigge 2002](#)), but also includes substantial detail on the ‘macro-atom’ technique, which was proposed by Leon Lucy and incorporated into PYTHON by Stuart Sim for a study on young-stellar objects ([Sim et al. 2005](#)). Although I have put significant effort into testing, fixing and developing this scheme, I did not write the original code to deal with macro-atoms in PYTHON.

Chapter 4, 5 and 6 were studies I led under the guidance of my supervisor. For these chapters I conducted all simulations and data analysis, produced all the figures and wrote the text. A publication based on chapter 6 is in preparation, and chapters 4 and 5 are based on the following papers:

- Chapter 4: Matthews J. H., Knigge C., Long K. S., Sim S. A., Higginbottom N., ‘The impact of accretion disc winds on the optical spectra of cataclysmic variables’, 2015, MNRAS, 450, 3331.
- Chapter 5: Matthews J. H., Knigge C., Long K. S., Sim S. A., Higginbottom N., Mangham S. W., ‘Testing quasar unification: radiative transfer in clumpy winds’, 2016, MNRAS, 458, 293.

The following additional publications are not included in this thesis, although some of the work presented here did contribute towards the respective results

- Higginbottom N., Knigge C., Long K. S., Sim S. A., Matthews J. H., ‘A simple disc wind model for broad absorption line quasars’, 2013, MNRAS, 436, 2.3
- Higginbottom, N., Proga D., Knigge C., Long K. S., Matthews J. H., Sim S. A., ‘Line-driven Disk Winds in Active Galactic Nuclei: The Critical Importance of Ionization’ and Radiative Transfer, 2014, ApJ, 789, 1.
- Shankar F., Calderone G., Knigge C., Matthews J. H., et al., ‘The OpticalUV Emissivity of Quasars: Dependence on Black Hole Mass and Radio Loudness’, 2016, ApJ Letters, 818, 1.

Signed:

---

Date:

---

## *Acknowledgements*

First and foremost, I would like to thank Christian Knigge, for being such an enthusiastic, helpful and stimulating supervisor throughout my PhD. Christian, I *always* left our meetings more positive than before – that speaks volumes – and I greatly enjoyed our conversations about science and Explosions in the Sky. I am also extremely grateful to Knox Long for all his assistance, writing the majority of the code and sharing some of his astronomy knowledge with me, and Stuart Sim for being immensely helpful throughout, especially when it comes to radiative transfer. I would also like to thank Nick Higginbottom for hours upon hours of assistance and friendship, and Sam Mangham for his help and input nearer the end of my PhD. To all of the above people; thank you for being part of a collaboration that does some great science, but also knew when to discuss a disastrous code bug with a knowing smile and ironic joke. I would also like to thank Daniel Proga, Omer Blaes, Ivan Hubeny, Shane Davis, Mike Brotherton, Mike DiPompeo, Frederic Marin, Daniel Capellupo, Dirk Grupe, Simo Scaringi, Adam Foster, Randall Smith, Chris Done, Anna Pala, Boris Gaensicke, Patrick Woudt and countless others for useful correspondence or stimulating scientific conversations. I am also very grateful to my masters supervisor Rosanne Di Stefano for inspiring me to continue doing research beyond my year in Boston.

Apart from those who I worked with, I am grateful to everyone who helped make Southampton a happy place to be over 3+ years. There are too many to name, but I will indulge a few. To my girlfriend Cat, thank you for being so patient with me and for so many lovely evenings. To Sam Connolly, you have been an ever-present and someone who I can always rely on for good beer, music and knowing looks. Sadie Jones, you were there when I needed you most for a cwtch or wanted to hear you pronounce year or ear. To Rob, Aarran, Juan, Georgios and Poppy, thanks for being true friends throughout the process. Big thanks to everyone else in the department for making it a super cool place to work, my office mates Mari, Judith, Stew and CFro, and my housemates Rich, Stu, Ollie, Sophie and Szymon. Thanks also goes to all the staff for being so friendly and approachable, particularly Poshak, Diego and Seb who have all helped me at various points through the PhD, and to Phil Charles for his sage advice since the early days.

There are also many people, outside of Southampton, who I must thank. Most of all, Mum, Dad, Beth and Nick, and the rest of my family. Thanks for supporting me

throughout my studies and just being all round lovely people. Thank you Josh, James and Alex, and our now manager John, for allowing me to play music that I love in Waking Aida. Eschaton and Full Heal were both released during my PhD, and in many ways they are each a thesis within themselves.

This work was supported by the Science and Technology Facilities Council via a 3.5 year PhD studentship. This work made use of the Sloan Digital Sky Survey. Funding for the Sloan Digital Sky Survey has been provided by the Alfred P. Sloan Foundation, the U.S. Department of Energy Office of Science, and the Participating Institutions. I acknowledge the use of the IRIDIS High Performance Computing Facility, and associated support services at the University of Southampton, in the completion of this work. Figures were produced using the `matplotlib` plotting library.

# Abbreviations

AGN	Active galactic nuclei/nucleus
ADAF	Advection dominated accretion flow
BAL	Broad absorption line
BALQSO	Broad absorption line quasar
BBB	Big blue bump
BEL	Broad emission line
BH	Black hole
BI	Balnicity index
BL	Boundary Layer
BLR	Broad line region
CDF	Cumulative distribution function
CGS	Centimetre-gram-second
CV	Cataclysmic variable
DN(e)	Dwarf nova(e)
EW	Equivalent width
HERG	High excitation radio galaxy
HMXB	High-mass X-ray binary
HSE	Hydrostatic Equilibrium
IP	Intermediate polar
IR	Infra-red
ISCO	Innermost stable circular orbit
LHS	Left-hand side
LINER	Low ionization nuclear emission-line region
LMXB	Low-mass X-ray binary
LTE	Local thermodynamic equilibrium
MCRT	Monte Carlo radiative transfer

MRI	Magneto-Rotational Instability
NAL	Narrow absorption line
NEL	Narrow emission line
NLR	Narrow line region
NL	Nova-like variable
NS	Neutron Star
QSO	Quasa-stellar object / Quasar
RL	Radio-loud
RHS	Right-hand side
RIAF	Radiatively inefficient accretion flow
RLOF	Roche lobe overflow
SA	Sobolev approximation
SED	Spectral energy distribution
SFR	Star formation rate
sSFR	Specific star formation rate
SMBH	Supermassive black hole
SXSS	Soft X-ray excess
UFO	Ultra-fast outflow
UV	Ultraviolet
WA	Warm absorber
WD	White dwarf
WHIM	Warm, highly ionized medium
XRB	X-ray binary
YSO	Young stellar object

# Physical Constants

Speed of light	$c = 2.997\ 924\ 58 \times 10^{10} \text{ cm s}^{-1}$
Boltzmann constant	$k = 1.380\ 658 \times 10^{-16} \text{ erg K}^{-1}$
Gravitational constant	$G = 6.672\ 599 \times 10^{-8} \text{ cm}^3 \text{ g}^{-1} \text{ s}^{-2}$
Solar mass	$M_{\odot} = 1.988\ 550 \times 10^{33} \text{ g}$
Solar radius	$L_{\odot} = 6.957\ 000 \times 10^{10} \text{ cm}$
Thomson cross-section	$\sigma_T = 6.652\ 458 \times 10^{-25} \text{ cm}^2$
Planck constant	$h = 6.626\ 076 \times 10^{-27} \text{ cm}^2 \text{ g s}^{-1}$
Stefan-Boltzmann constant	$\sigma = 5.670\ 367 \times 10^{-5} \text{ erg cm}^{-2} \text{ K}^{-4} \text{ s}^{-1}$
Parsec	$pc = 3.085\ 678 \times 10^{18} \text{ cm}$
Proton mass	$m_p = 1.672\ 621 \times 10^{-24} \text{ g}$
Electron mass	$m_e = 9.109\ 390 \times 10^{-28} \text{ g}$
Electron volt	$eV = 1.602\ 177 \times 10^{-12} \text{ erg}$
Electron charge	$q_e = 4.803\ 207 \times 10^{-10} \text{ esu}$
$\pi$	$= 3.141\ 593$
$e$	$= 2.718\ 282$

All constants are given to 6 decimal places, except for the speed of light which is exact. Throughout this thesis I use the centimetre-gram-second (CGS) system of units unless otherwise stated.



*Dedicated to my family.*



# Chapter 1

## Introduction

“And now you’re asking, I don’t know where to begin”

*Mike Vennart, Silent/Transparent*

The release of gravitational potential energy as mass falls towards a compact object is the most efficient energetic process in the universe, even more efficient than nuclear fusion. This *accretion* process is thought to power the huge radiative engines at the centres of many galaxies – accreting supermassive black holes known as active galactic nuclei (AGN). As the matter falls into the potential well of the black hole, it often forms an accretion disc. This disc is an efficient radiator of the gravitational potential energy released and can sometimes outshine the entire stellar population of the galaxy, appearing as a quasi-stellar object (QSO) or *quasar*. As well as powering AGN, accretion discs are present in X-ray binaries (XRBs), young-stellar objects (YSOs) and cataclysmic variables (CVs). Accretion is a universal process; broadly speaking, the physics is similar regardless of whether matter is falling on to a  $\sim 1 M_{\odot}$  neutron star or white dwarf, or a  $\sim 10^{10} M_{\odot}$  black hole.

Outflows are ubiquitous in accreting systems. We see collimated radio jets in AGN (Hazard et al. 1963; Potash & Wardle 1980; Perley et al. 1984; Marscher 2006) and XRBs (Belloni 2010), and there is even evidence of radio emission in CVs (Benz et al. 1983; Körding et al. 2008; Coppejans et al. 2015). These radio jets tend to appear in specific accretion states (Fender 2001; Fender et al. 2004; Körding et al. 2008), implying an intrinsic connection to the accretion process. Even more intriguing, less collimated,

mass-loaded outflows or *winds* are observed in XRBs in soft accretion states, possibly emanating from the accretion disc (Ponti et al. 2012). Evidence for disc winds is widespread across the mass range, but perhaps the most spectacular indication is the blue-shifted, broad absorption lines (BALs) in the rest-frame ultraviolet (UV) seen in high-state CVs (Heap et al. 1978; Greenstein & Oke 1982; Cordova & Mason 1982) and in the so-called broad absorption line quasars (BALQSOs) that make up 20% – 40% of quasars (Weymann et al. 1991; Knigge et al. 2008; Allen et al. 2011). BALs and ‘P-Cygni’ profiles (Struve 1935; Rottenberg 1952) are also seen in stellar winds (e.g. Cassinelli 1979) and sometimes even in the optical spectra of CVs (Patterson et al. 1996; Ringwald & Naylor 1998; Kafka & Honeycutt 2004). Broad, blue-shifted absorption is also observed in the Fe K $\alpha$  line in some AGN (Reeves et al. 2003; Pounds & Reeves 2009; Tombesi et al. 2010) – these are known as ultra-fast outflows or UFOs.

The astrophysical significance of AGN disc winds extends, quite literally, far beyond the accretion environment. They offer a potential mechanism by which the central accretion engine can interact with the host galaxy and interstellar medium via a ‘feedback’ mechanism (King 2003; Fabian 2012). Feedback is required in models of galaxy evolution (Springel et al. 2005) and may explain the famous ‘ $M_{BH} - \sigma_*$ ’ (Silk & Rees 1998; Häring & Rix 2004) and ‘ $M_{BH} - M_{bulge}$ ’ (Magorrian et al. 1998) relations. Winds also offer a natural way to *unify* much of the diverse phenomenology of AGN, CVs and XRBs. This principle of unification can be applied along more than one ‘axis’ of parameter space. For example, there exist elegant models that attempt to explain *all* of the behaviour of quasars with only a central black hole, a jet, an accretion disc, and an associated outflow, just by varying the viewing angle (Elvis 2000). Similarly elegantly, it has been shown that much of the behaviour of XRBs is directly analogous to AGN (McHardy et al. 2006), and models of outflows in CVs have been successfully ‘scaled-up’ and applied to quasars and AGN (e.g. Higginbottom et al. 2013).

Despite their importance and ubiquity, there are still many unanswered questions relating to the true impact of winds and their underlying physical origins. Here, I aim to address some of these questions and take steps towards building a more holistic picture of the impact of winds on the spectral appearance and accretion physics of disc systems. This thesis is structured as follows. In the remainder of this chapter, I will outline the background accretion theory and highlight the successes and failures of accretion disc models when compared to observations, as well as describing the different classes

of accreting objects in more detail. In chapter 2, I dedicate some time to specifically discussing the theory of, and observational evidence for, accretion disc winds. In chapter 3, I outline the Monte Carlo radiative transfer and photoionization methods I have used in order to investigate the impact of disc winds on the spectra of accreting systems. The next three chapters are based on two publications and one paper in preparation, in which I discuss the impact of disc winds on the spectra of CVs (Chapter 4), and test disc wind quasar unification models (Chapters 5 and 6). In chapter 7, I summarise my findings and their astrophysical significance, and discuss potential avenues for future work.

## 1.1 The Physics of Accretion

The basic phenomenon of accretion – matter falling into a gravitational potential well – is ubiquitous in astrophysics. The energy,  $\Delta E$ , released by a parcel of mass,  $\Delta m$ , falling from infinity onto an object of mass  $M$  and radius  $R_*$  is given by

$$\Delta E = \frac{GM\Delta m}{R_*}, \quad (1.1)$$

meaning that the power generated by mass accreting at a rate  $\dot{M}$  onto this object is given by

$$L_{\text{acc}} = \frac{GM\dot{M}}{R_*}. \quad (1.2)$$

We can also characterise the efficiency of any energetic process by relating the energy released to the rest mass energy of the parcel of mass, such that

$$\Delta E = \eta\Delta mc^2, \quad (1.3)$$

where  $\eta$  is the radiative efficiency. Similarly, in terms of luminosity,  $L$ ,

$$L = \eta\dot{M}c^2. \quad (1.4)$$

Nuclear fusion is one of the more efficient energetic processes in the universe, with an efficiency of  $\eta = 0.007$ . If we rearrange the above equations in terms of  $\eta$ , we find

$$\eta = \frac{G}{c^2} \frac{M}{R_*}. \quad (1.5)$$

Object	$M(M_\odot)$	$R_*(R_\odot)$	$M/R_*(M_\odot/R_\odot)$	$\eta$
White Dwarf	0.8	0.01	79.4	$1.6 \times 10^{-4}$
Neutron Star	1.4	$1.4 \times 10^{-5}$	$10^5$	0.2
Black Hole	10	$4.2 \times 10^{-6}$	$2.4 \times 10^5$	0.5
SMBH	$10^9$	4244	$2.4 \times 10^5$	0.5

TABLE 1.1: Approximate values of compactness and accretion efficiency for four different compact objects with typical parameters. Here,  $R_*$  for black holes is set to the event horizon for a Schwarzschild black hole, whereas values of  $\eta \approx 0.1$  in discs are more realistic due to the presence of an innermost stable orbit (see section 1.1.3). SMBH stands for supermassive black hole.

In other words, the efficiency of accretion is directly related to the *compactness*,  $M/R_*$ , of the central object. Values of compactness and the associated radiative efficiencies for four different compact objects are shown in table 1.1.

### 1.1.1 Spherical Accretion and The Eddington Limit

The simplest geometry one might propose for accretion would be one in which a central mass accretes matter in a spherically symmetric manner. The process of spherical accretion has come to be known as Bondi-Hoyle-Lyttleton accretion ([Hoyle & Lyttleton 1939](#); [Bondi & Hoyle 1944](#)). In particular, [Bondi \(1952\)](#) studied spherically symmetric accretion onto a point mass and derived the Bondi radius,

$$r_B = \frac{GM}{c_S^2}, \quad (1.6)$$

where  $c_S = c_S(r_B)$  is the sound speed as a function of radius. The Bondi radius represents a critical point inside which the material is supersonic and will accrete on the free-fall timescale,  $\tau_{\text{ff}}$ . For a cloud of uniform density,  $\rho_0$ , this is given by

$$\tau_{\text{ff}} = \sqrt{\frac{3\pi}{32G\rho_0}}. \quad (1.7)$$

When this timescale is long enough, the accreting matter can radiate away its potential energy, generating a luminosity  $L$ . This radiation will exert a force on the electrons at radius  $r$  in the cloud, given by

$$F_{\text{rad}} = \frac{L\sigma_T}{4\pi r^2 c}, \quad (1.8)$$

where  $\sigma_T = 6.65 \times 10^{-25} \text{ cm}^2$  is the Thomson cross-section. If this outward radiation force dominates over the inward pull of gravity, the material will no longer fall inwards. Consider radiation pressure acting on ionized hydrogen, for which the gravitational force

is approximately given by  $F_G \approx GMm_p/r^2$ . Combining this expression with equation 1.8 gives a natural maximum accretion luminosity, known as the *Eddington limit*, of

$$L_{\text{Edd}} = \frac{4\pi GMm_p c}{\sigma_T}, \quad (1.9)$$

with an associated Eddington accretion rate of

$$\dot{M}_{\text{Edd}} = \frac{L_{\text{Edd}}}{\eta c^2}. \quad (1.10)$$

The Eddington limit depends on a number of assumptions, namely that the accretion flow is steady, spherically symmetric, ionized, and that its opacities are dominated by electron scattering. Clearly, there are many astrophysical situations where one or more of these assumptions do not hold. For example, the recent outburst of V404 Cyg showed wildly variable luminosities on short timescales (see, e.g., [Kuulkers et al. 2015](#); [Motta et al. 2015](#), among many, many ATels), and in any binary or disc dominated system the assumption of spherical symmetry will break down. Nevertheless, the Eddington limit provides a good order of magnitude estimate of the maximum luminosity of an accreting object, and also provides a useful way of parameterising accretion rates, as it scales linearly with mass. It can also be used to characterise the *state* of an accretion flow. In general, sources above  $\sim 0.1 L_{\text{Edd}}$  find themselves in a ‘soft’ or thin-disc state (see section 1.1.2.1), whereas for much lower Eddington fractions, sources are expected to harbour geometrically thick, advection-dominated accretion flows (ADAFs; [Narayan & Yi 1994, 1995](#)) or, more generally, radiatively inefficient accretion flows (RIAFs). It is also clear that, near the Eddington limit, radiation pressure must play a major role in determining the disc morphology (see section ??).

### 1.1.2 Accretion Discs

In many astrophysical situations – for example, in binary systems and gas clouds orbiting BHs – any accreting matter will possess some net angular momentum. If the medium is dense enough, collisions between particles will be frequent, but the total angular momentum vector of two colliding particles will always be conserved. This provides a mechanism for a gas cloud to relax to its minimum energy state – an accretion disc.

As well as losing gravitational potential energy as it falls towards the central mass, a parcel of matter must also lose its angular momentum. Crucially, accretion discs

provide a way for this to happen. If the disc overall maintains the same total angular momentum, it follows that angular momentum must be transported outwards within the disc. The mechanism for transporting angular momentum outwards is unknown, and this is one of the biggest weaknesses of current accretion disc theory. Traditional molecular viscosity is insufficient in this regard (Pringle 1981). The reasons for this are readily apparent when we consider that molecular viscosity operates over the Debye length,  $\lambda_D$ , and at the sound speed,  $c_s$ . At density  $\rho$ , this results in a viscous force density ( $\sim \rho \lambda_D c_s v_\phi / R^2$ ) that is much lower than the inertial force density ( $\sim \rho v_\phi^2 / R$ ). In other words, the Reynolds number is much greater than 1. The consequence is that molecular viscosity is dynamically unimportant in accretion flows.

An alternative mechanism for angular momentum transport is therefore necessary. The most commonly invoked candidate is the magnetorotational instability (MRI; Balbus & Hawley 1991), in which accretion discs are subject to a strong shearing instability even when the magnetic field is weak. Angular momentum could also be lost via a magnetohydrodynamic outflow (Blandford & Payne 1982) or transported by spiral shock waves (Ju et al. 2016), although in the former case the disc would actually be dark if a wind extracted all the angular momentum (e.g. Spruit 1996; Knigge 1999). Given the uncertainty about the transport mechanism, it is convenient to simply parameterise the unknown physics in an *effective viscosity*.

### 1.1.2.1 Steady-state Accretion Discs: the $\alpha$ -prescription

The so-called  $\alpha$ -disc model developed by Shakura & Sunyaev (1973, hereafter SS73) and Lynden-Bell (1969) is a simple approximation for how energy and angular momentum are transported in an accretion disc and provides useful insights into the disc's expected observational appearance. The starting point for this model is a parameterisation of the viscosity,  $\nu'$ , using the simple form

$$\nu' = \alpha c_s H, \quad (1.11)$$

where  $H$  is the scale height of the disc,  $\alpha$  is a parameter  $\leq 1$ , and  $c_s$  is the sound speed. Viscous torques then allow the conversion of orbital kinetic energy into heat, which can be radiated away. If we make one further assumption, that the accretion rate is constant throughout the disc, we can write down a mass continuity equation valid at any radius,

given by

$$\dot{M} \equiv 2\pi R v_R \Sigma = \text{constant}, \quad (1.12)$$

where  $\Sigma$  is the surface density at that radius and  $v_R$  is the radial ‘drift’ velocity towards the compact object. The angular momentum equation then becomes

$$\nu' \Sigma = \frac{\dot{M}}{3\pi} \left[ 1 - \left( \frac{R}{R_*} \right)^{1/2} \right]. \quad (1.13)$$

The viscous torques throughout the disc cause a local loss of mechanical energy, allowing us to derive (see, e.g. Frank et al. 1992) a rate of viscous dissipation, per unit area, given by

$$D(R) = \frac{1}{2} \nu' \Sigma (R \Omega')^2. \quad (1.14)$$

Here,  $D(R)$  is proportional to the derivative of the angular velocity,  $\Omega' = d\Omega/dR$ . By combining equations 1.14 and 1.13, we can show that the viscous dissipation rate is

$$D(R) = \frac{GM\dot{M}}{8\pi R^3} \left[ 1 - \left( \frac{R}{R_*} \right)^{1/2} \right], \quad (1.15)$$

where we have also set the angular velocity to the Keplerian velocity. This expression is independent of viscosity – which is fortunate, because we do not know what value of  $\alpha$  to use in equation 1.11. This result comes about because of the implicit assumption that the viscosity regulates the mass accretion rate so as to achieve a steady state.

We can now integrate across both sides of the whole disc to obtain the disc luminosity,

$$L_{\text{disc}} = 2 \int_{R_*}^{\infty} D(R) 2\pi R dR = \frac{GM\dot{M}}{2R_*} = \frac{1}{2} L_{\text{acc}}. \quad (1.16)$$

This result can also be shown by considering the difference in gravitational binding energy of gas in Keplerian rotation at  $R = R_*$  and  $R = \infty$ . From equation 1.15, an effective temperature distribution can be derived by setting

$$\sigma T_{\text{eff}}^4(R) = D(R), \quad (1.17)$$

which then gives

$$T_{\text{eff}}(R) = T_* \left[ 1 - \left( \frac{R}{R_*} \right)^{1/2} \right]^{1/4}, \quad (1.18)$$

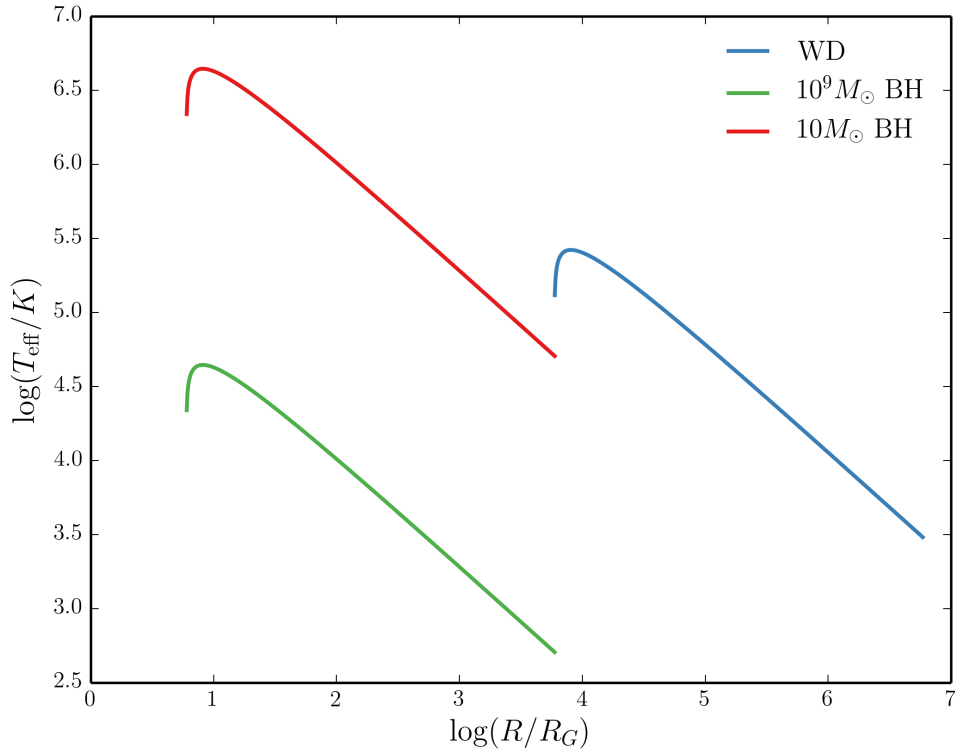


FIGURE 1.1: The temperature profile of an accretion disc for three different classes of compact object.

where

$$T_* = \left( \frac{3GM\dot{M}}{8\pi R_*^3 \sigma} \right)^{1/4}. \quad (1.19)$$

When  $R \gg R_*$  this simplifies to

$$T_{\text{eff}}(R) = T_*(R/R_*)^{-3/4}. \quad (1.20)$$

Now we have not only derived the total luminosity of an accretion disc, but also the effective temperature profile which will govern the shape of the emergent SED. This temperature profile is shown in Fig. 1.1 for three different compact objects, assuming an Eddington fraction of 0.2.

### 1.1.3 Boundary Layers, Black Hole Spin and the ISCO

In equation 1.16, we found that  $L_{\text{disc}} = 1/2 L_{\text{acc}}$ . One might then ask: where does the rest of the luminosity go? Alternatively, what happens to the kinetic energy the material has at the inner disc edge? The answer is dependent on the compact object in

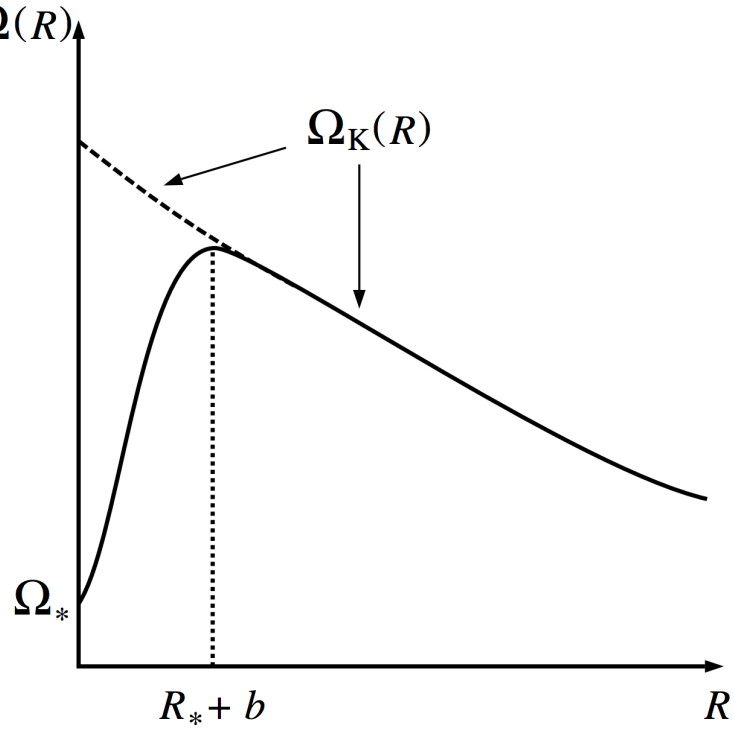


FIGURE 1.2: Credit: Frank et al. 2002. Angular velocity as a function of radius in an accretion disc around a rotating compact object with angular velocity  $\Omega_*$ .  $\Omega_K$  is the Keplerian angular velocity. This graph also helps explain why there is a turnover in the temperature-radius relation, as  $D(R)$  is proportional to the square of the derivative of this quantity.

question. In an accreting WD, the rotating matter must eventually deposit itself on the surface of the WD. This is illustrated in Fig. 1.2, which shows the angular velocity as a function of radius in a disc around a compact object rotating with angular velocity  $\Omega_*$ . The boundary layer (BL) is the region to the left of the dotted line, inside the maximum of  $\Omega$ , the angular velocity. The luminosity of the boundary layer is (Frank et al. 1992)

$$L_{BL} = \frac{1}{2} \frac{GM\dot{M}}{R} \left[ 1 - \left( \frac{\Omega_*}{\Omega_K(R_*)} \right) \right]^2, \quad (1.21)$$

where  $\Omega_K(R_*)$  is the Keplerian angular velocity at  $R_*$ , assuming the thickness,  $b$ , of the BL is small. When  $\Omega_K(R_*) \gg \Omega_*$ , this reduces to  $L_{BL} = 1/2 L_{acc} = L_{disc}$ . Any remaining energy is imparted to the WD as rotational energy.

In cataclysmic variables, BLs can be approximated with blackbodies and their temperatures estimated indirectly via the Zanstra (1929) method (e.g. Hoare & Drew 1991, 1993). However, they likely exhibit a variety of atomic features (Suleimanov et al. 2014). Extreme-UV (EUV) datasets have confirmed the existence of boundary layer emission in non-magnetic CVs (Mauche 1996), although these observations are limited in number.

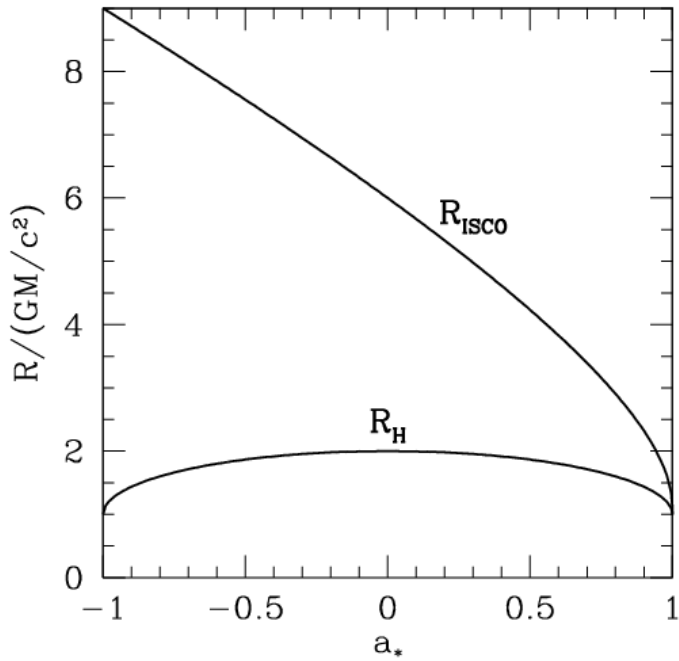


FIGURE 1.3: Credit: Narayan 2014. The radius of the ISCO,  $R_{ISCO}$ , and the horizon,  $R_H$ , is as a function of the BH spin parameter,  $a_*$ .  $a_* = 0$  corresponds to a Schwarzschild BH, and  $a_* = 1$  and  $a_* = -1$  to prograde and retrograde Kerr BHs respectively. Note that this figure ignores the counteracting torque of photons swallowed by the BH, which actually limits  $a_*$  to a value of around 0.998 (Thorne 1974).

Clearly, in BH systems a boundary layer cannot exist in the same way, due to the lack of a physical surface. Instead, the energy must either go into growing the BH, contributing to its angular momentum or being channeled into a jet or other radiative source (see section 1.5.2). The question of what happens at the inner disc edge is complicated further by the fact that the disc cannot extend to the event horizon of the BH. Instead, there is an ‘innermost stable circular orbit’ (ISCO) beyond which the accreting matter will simply fall into the BH along nearly radial paths. The radius of this orbit,  $R_{ISCO}$ , and the horizon radius,  $R_H$ , is shown for different values of the BH spin parameter,  $a_*$ , in Fig. 1.3, showing how matter can orbit closer to a prograde spinning BH. In estimating the luminosity of a Keplerian disc around a BH, we should really set  $R_* = R_{ISCO}$  in equation 1.5, giving the interesting result that rapidly spinning (Kerr) BHs ( $\eta \approx 0.32$ ) are more radiatively efficient than Schwarzschild BHs ( $\eta \sim 0.17$ ).

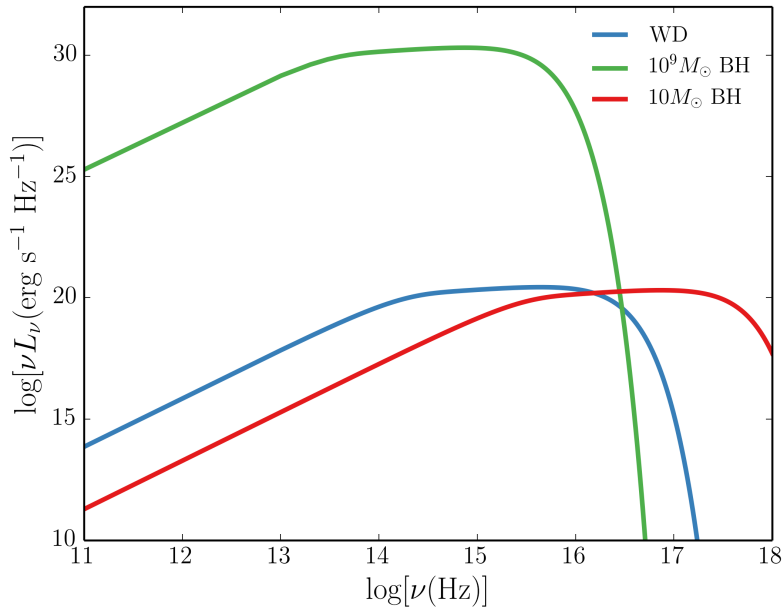


FIGURE 1.4: Accretion disc SEDs for three different compact objects, corresponding roughly to a quasar, an XRB and a CV. The SEDs are computed via an area-weighted sum of blackbodies with effective temperatures governed by equation 1.18, and the  $\nu^{1/3}$  shape in the middle of the spectra can be seen.

#### 1.1.4 The Emergent Spectrum

It is important to recognise that the steady-state disc treatment *does not specify the exact shape of the disc SED*. What it does do is say where energy is originally released. The simplest assumption is that each annulus emits as a blackbody with temperature  $T_{\text{eff}}(R)$ , i.e. that the specific intensity through the emitting surface follows Planck's law:

$$B_{\nu}(T) = \frac{2h\nu^3}{c^2} \frac{1}{\exp(h\nu/kT) - 1}. \quad (1.22)$$

Under this assumption, it is possible to show that at intermediate frequencies, where  $kT(R_{max}) \ll h\nu \ll kT_*$ , the spectrum appears as a ‘stretched blackbody’, with monochromatic flux,  $F_{\nu}$ , of the form

$$F_{\nu} \propto \nu^{1/3}. \quad (1.23)$$

Fig. 1.4 shows the blackbody SEDs expected for the same objects as in Fig. 1.1, in which the  $\nu^{1/3}$  portion can be clearly seen. A stellar atmosphere model with frequency-dependent opacity creates a somewhat different (and more realistic) spectrum. Fig. 1.5 shows a comparison between a disc spectrum computed with stellar atmosphere models and standard multi-temperature blackbody disc, showing how the two treatments

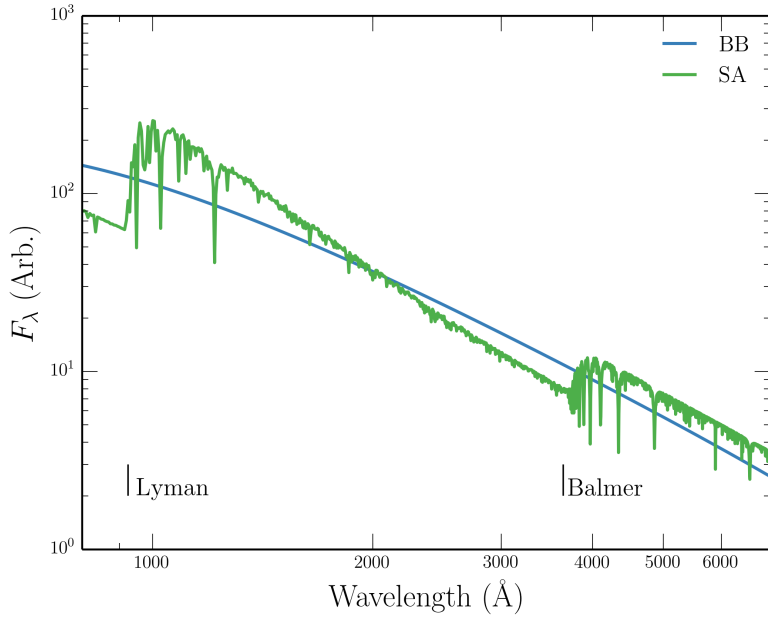


FIGURE 1.5: A comparison between a disc spectrum computed with stellar atmosphere models and standard multi-temperature blackbody disc. The major photoabsorption edges are marked. Flux is reprocessed into different wavelengths by bound-free opacities, and line blanketing also has a big effect on the spectrum. The Hydrogen and Helium lines also experience a degree of pressure broadening.

can have a significantly different spectral shape when one includes frequency-dependent opacities in the atmosphere. It is of course possible that *neither* a blackbody treatment or the current stellar atmosphere models produce accurate disc spectra. I shall therefore devote a little time to discussing the observational appearance of accretion discs and reviewing the different classes of accreting objects.

## 1.2 Accreting Compact Binaries

Accreting compact binaries form many different classes, but all are characterised by matter streaming from a donor onto a compact object. When the compact object is more massive than the donor, it is designated as the ‘primary’, and its companion as the ‘secondary’. In high-mass X-ray binaries (HMXBs), the opposite is formally true. There are only two ways by which matter can transfer from the secondary to the compact object. One is by Roche lobe-overflow (RLOF), where the donor star expands to fill its Roche lobe, a critical surface of equipotential around the star (see section 1.2.1). The alternative is that the donor may expel material in an outflow, some of which can be captured by the compact object. Although accretion from a wind or circumstellar disc

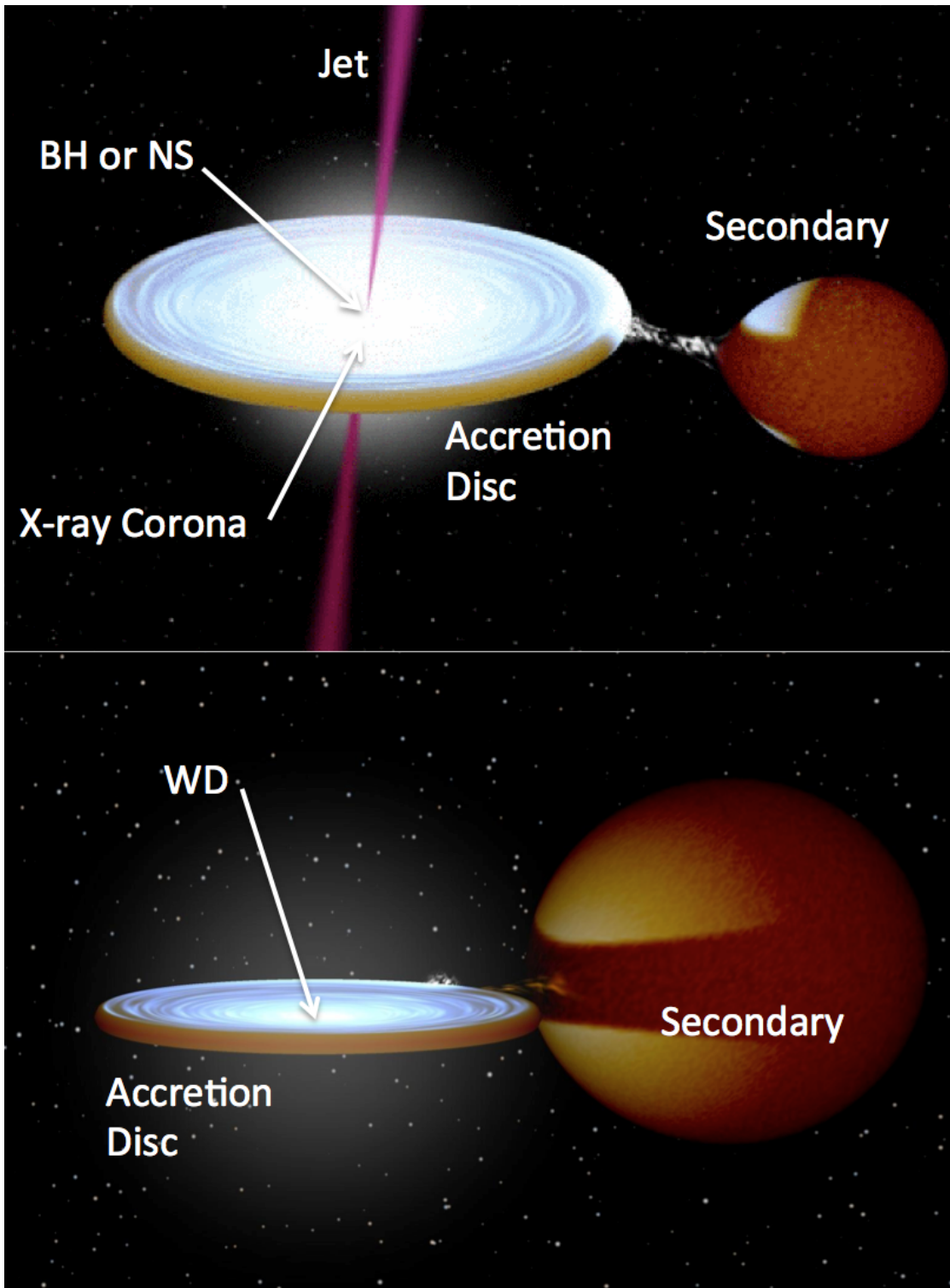


FIGURE 1.6: Credit: Rob Hynes. Artists impression of a low-mass X-ray binary (top) and cataclysmic variable (bottom). The key components are marked, and the clear similarity in overall structure is apparent.

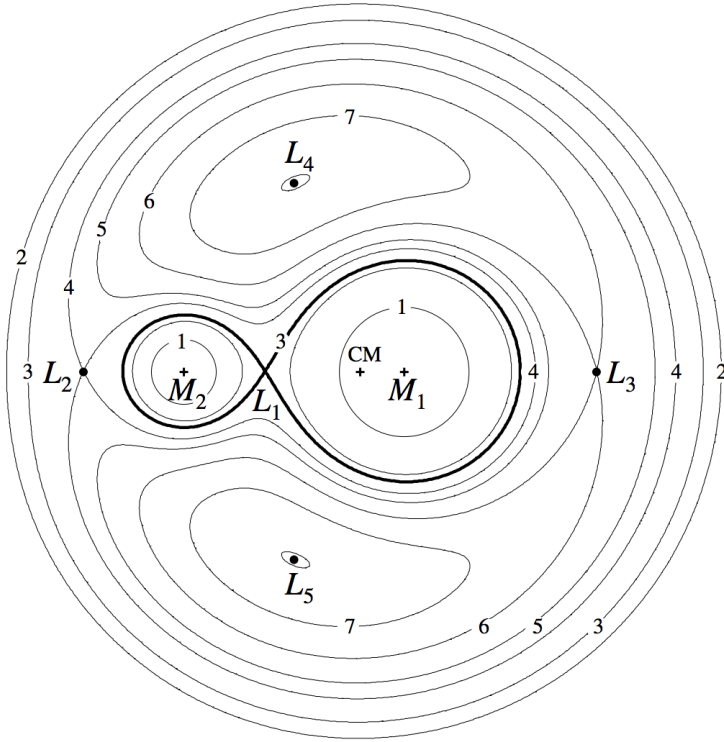


FIGURE 1.7: Credit: Frank et al. 2002. The Roche potential in a binary system for  $q_M = M_2/M_1 = 0.25$ . The Lagrangian points are marked, as are the locations of the individual and system centres of mass.

is common in HMXBs (Bartlett 2013), here I will focus on RLOF as it is more common in the systems that possess high-state accretion discs and associated outflows. Two examples of these are shown in Fig. 1.6

### 1.2.1 Roche Lobe-Overflow

Let us consider a binary system containing two point sources with masses  $M_1$  and  $M_2$  at positions  $\vec{r}_1$  and  $\vec{r}_2$ . The Roche potential,  $\Phi_R$ , in this system is then

$$\Phi_R = -\frac{GM_1}{|\vec{r} - \vec{r}_1|} - \frac{GM_2}{|\vec{r} - \vec{r}_2|} - 1/2(\vec{\omega} \times \vec{r})^2, \quad (1.24)$$

where  $\vec{\omega}$  is the angular velocity of the binary and is a vector normal to the orbital plane. This potential is plotted in Fig. 1.7 for a mass ratio,  $q_M = M_2/M_1 = 0.25$ .

In the context of semi-detached binary systems, the most important equipotential is the dumbbell-shaped region enclosing both masses. Each of these enclosed regions is known as the ‘Roche lobe’ of the object. A good approximation for the size of the Roche lobe

takes the form (Eggleton 1983)

$$\frac{R_2}{a} = \frac{0.49q_M^{2/3}}{0.6q_M^{2/3} + \ln(1 + q_M^{1/3})}. \quad (1.25)$$

Here,  $R_2$  is the radius of a sphere with the same volume as the Roche lobe for the secondary star, which we can see depends only on  $q_M$  and the orbital separation,  $a$ . If this secondary expands enough to fill its Roche lobe, then matter will fall onto the other object through the  $L_1$  Lagrangian point. This process is known as Roche lobe overflow (RLOF) and is vitally important in astrophysics. Any accretion from RLOF will alter the mass ratio of the binary system and thus affects the evolution of binary systems. This is reflected in the orbital period distribution of binaries (e.g. Knigge et al. 2011) and also affects the delay time distribution of Type Ia Supernovae, for which CVs are one of the progenitor candidates (e.g. Wang & Han 2012). It is also worth noting that the existence of gravitational waves has been required in models to explain the orbital period evolution of CVs since the 1960s (Kraft et al. 1962).

### 1.2.2 Cataclysmic Variables

Cataclysmic variables (CVs) are systems in which a WD accretes matter from a donor star via Roche-lobe overflow (see the ‘CV bible’, Warner 2003). CVs are not always dominated by their accretion luminosity; for example, novae undergo dramatic eruptions caused by thermonuclear runaway, and the so-called ‘supersoft sources’ show evidence of nuclear burning on the WD surface. Accretion-dominated CVs – the focus here – can be classified according to the magnetic field strength of their WD primary ( $B_{WD}$ ) and their photometric activity. Magnetic systems are classified as either ‘Polars’ ( $B_{WD} \gtrsim 10^7$  G) or ‘Intermediate Polars’ (IPs;  $10^6 \lesssim B_{WD} \gtrsim 10^7$  G); in these systems the accretion flow inside the some critical radius (related to the Alfvén radius) is dominated by the WDs magnetic field. In polars, this radius is large enough, due to the strong magnetic field, that no disc forms at all (Liebert & Stockman 1985). In IPs the accretion disc is truncated at the magnetospheric boundary, and accretion ‘curtains’ channel the material onto the WD (e.g. Patterson 1994; Evans et al. 2004). When  $B_{WD} \lesssim 10^6$  G the accretion disc can extend all the way down to the WD boundary, and the CV is classified as non-magnetic. Here, I consider only non-magnetic CVs, which come in two flavours: dwarf novae and nova-like variables.

### 1.2.2.1 Dwarf Novae and the Disc-instability Model

Dwarf novae (DNe) are CVs that are characterised by repeated cycles of faint quiescence followed by a dramatic bright outburst. One of the most famous DNe is SS Cyg, whose light curve is shown in Fig. 1.8. The repeated outbursts can be clearly seen, and SS Cyg itself has been undergoing this behaviour over the full century for which it has been observed. A spectrum over the course of a typical outburst is shown in Fig. 1.9 and is characterised by the appearance of a blue, optically thick accretion disc continuum – note the similarity to the stellar atmosphere disc spectrum computed in section 1.1.2.1 and to the intermediate inclination nova-like variables discussed in the next section.

The leading scenario for explaining DN outbursts, and in fact also the outbursts in low mass X-ray binaries or ‘soft X-ray transients’, is the disc-instability model (DIM; [Osaki 1974](#); [Hōshi 1979](#); [Meyer & Meyer-Hofmeister 1981](#); [Lasota 2001](#)). In this model, the disc is in a cool, low viscosity state in quiescence, and H is mostly neutral. The constant mass supply from the donor causes a gradual build up of mass in the disc. Eventually, the disc hits a critical temperature, around 7000 K, and H becomes ionized. This causes an increase in viscosity and temporarily allows a higher accretion rate through the disc. In this state, the disc becomes geometrically thin and optically thick. It can now undergo efficient radiative cooling, meaning that a significant increase in brightness is observed. This state is relatively short-lived, as the accretion rate through the disc will be lower than the supply rate from the donor star, so eventually the disc will drop below the critical temperature and back onto the cool, low viscosity branch.

### 1.2.2.2 Nova-like Variables

Nova-like variables (NLs) are similar to DNe, except that the disc is always in a relatively high-accretion-rate state ( $\dot{M} \sim 10^{-8} M_{\odot} \text{ yr}^{-1}$ ). NLs are therefore one of the best ‘laboratories’ for testing the steady-state accretion disc theory described in section 1.1.2.1. In the optical, NLs generally exhibit a series of H and He emission lines superposed on a blue continuum. In many cases, and particularly in the SW Sex subclass of NLs ([Honeycutt et al. 1986](#); [Dhillon & Rutten 1995](#)), these lines are single-peaked. This is contrary to theoretical expectations for lines formed in accretion discs, which are predicted to be double-peaked ([Smak 1981](#); [Horne & Marsh 1986](#)). *Low-state* CVs (dwarf novae in quiescence) do, in fact, exhibit such double-peaked lines ([Marsh & Horne 1990](#)).

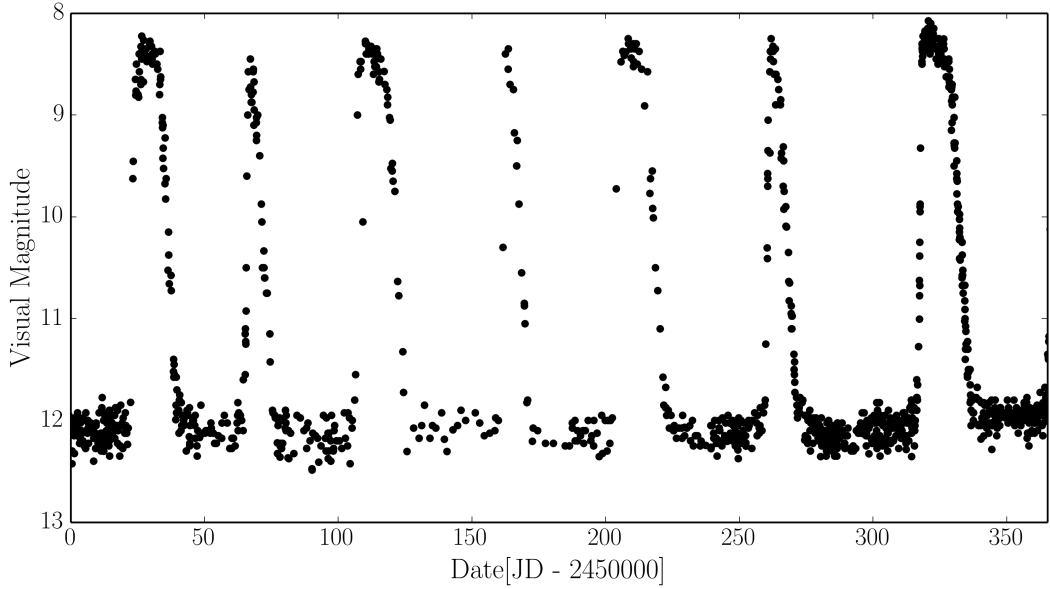


FIGURE 1.8: *Data: AAVSO.* A year in the life of SS Cyg, showing the characteristic repeated outbursts and periods of quiescence typical of a DN. SS Cyg has been undergoing this activity since it was first observed in 1896.

The UV spectra of NLs also show strong emission lines, and at low to intermediate inclinations dramatic blue-shifted absorption lines can be seen in some objects. The emission line equivalent widths in both the optical and the UV show clear trends with inclination (Hessman et al. 1984; Echevarria 1988; Noebauer et al. 2010). This can be seen clearly in Fig. 1.11 and is connected to the correlation between line strength and absolute magnitude found by Patterson (1984); that is, the decrease in equivalent width at low inclination is caused by an *increase* in continuum flux, rather than a decrease in line flux. This is discussed further in chapters 4 and 6, but also has relevance to AGN and quasar unification schemes mentioned later in this introduction. The optical and UV spectra of NL CVs are discussed further in the context of winds in chapter 2.

### 1.2.3 Low Mass X-ray Binaries

Although I do not study low-mass X-ray binaries (LMXBs) directly in this thesis, it is instructive to briefly discuss their observational appearance, as it is relevant to the connections between accretion and outflows. LMXBs are similar to CVs in structure (see Fig. 1.6), but the compact object is either a neutron star (NS) or a black hole (BH). The accretion disc emits in the soft X-ray regime, and an additional hard X-ray power law is also seen in the spectrum. This hard component is normally attributed to Compton up-scattering of seed disc photons by some kind of ‘corona’ of hot electrons

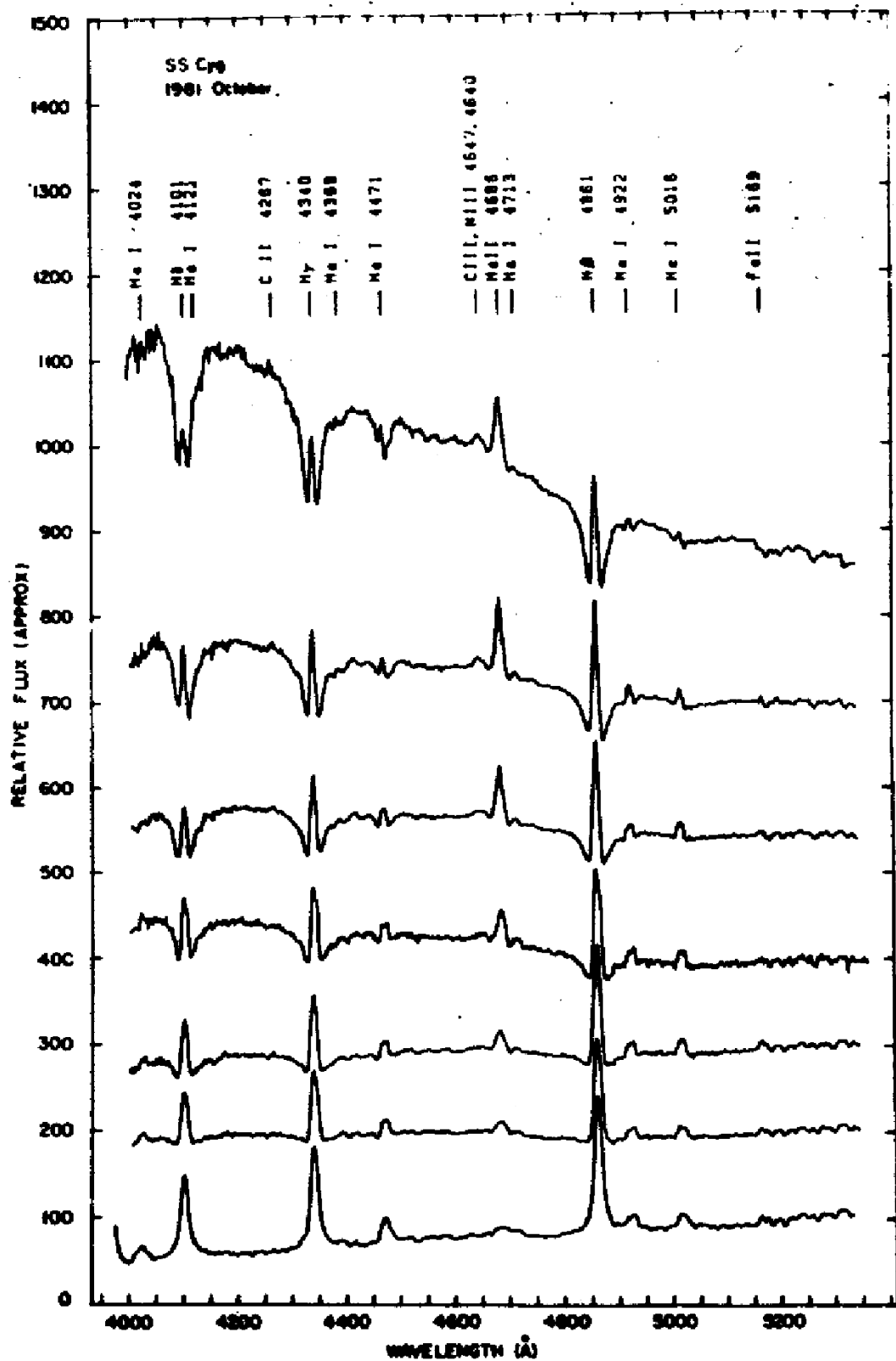


FIGURE 1.9: Credit: Hessman et al. 1984 / Dhillon et al. 1996. Spectra of SS Cyg during an outburst cycle, showing the evolution from minimum to maximum light. The rise is characterised by the appearance of an optically thick accretion disc spectrum. The flux scale is approximate.

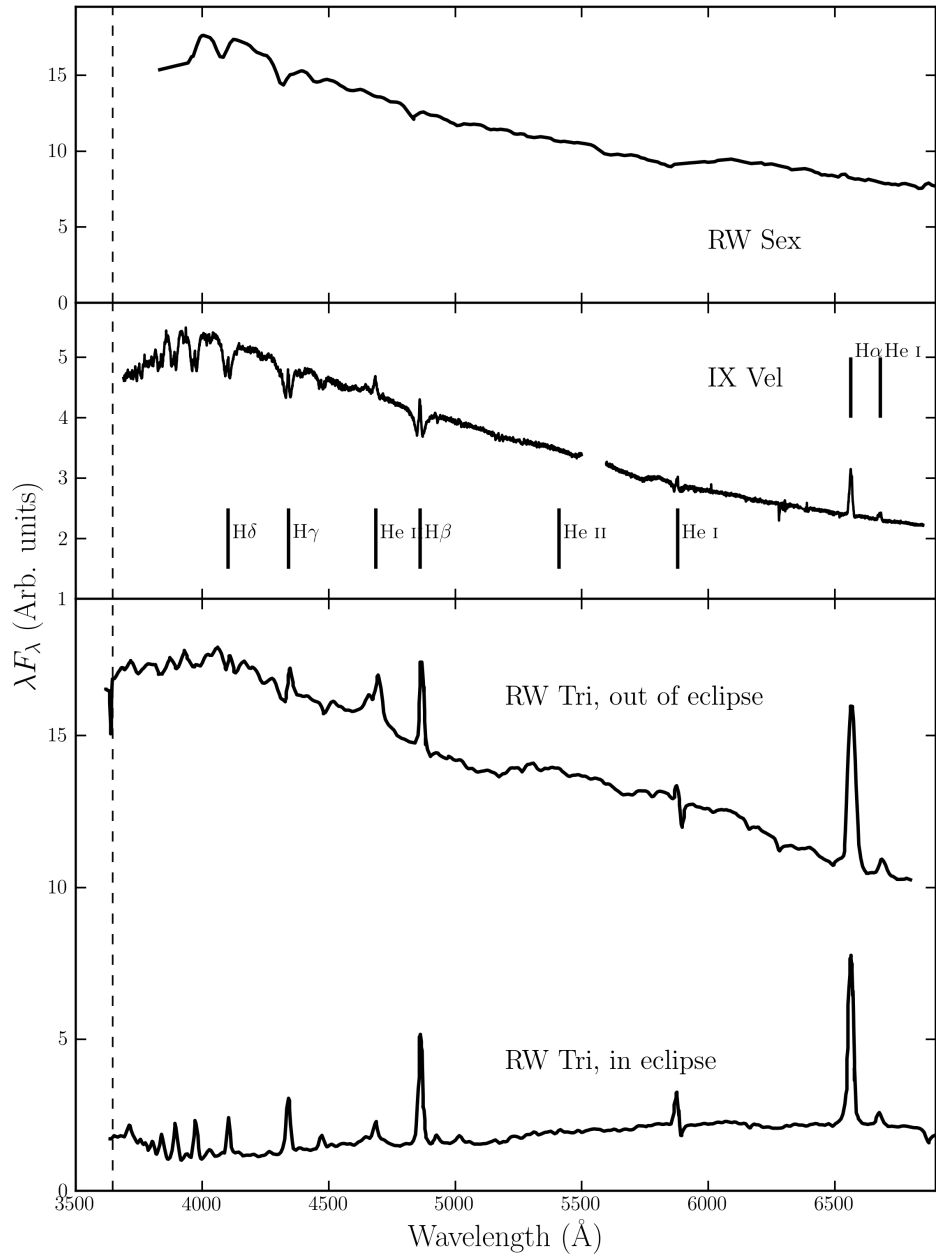


FIGURE 1.10: Optical spectra of three nova-like variables: RW Sex (top; Beuermann et al. 1992), IX Vel (top middle; A. F. Pala & B. T. Gaensicke, private communication) and RW Tri in and out of eclipse (bottom two panels; Groot et al. 2004). The data for RW Sex and RW Tri were digitized from the respective publications, and the IX Vel spectrum was obtained using the XSHOOTER spectrograph on the Very Large Telescope on 2014 October 10. These systems have approximate inclinations of  $30^\circ$ ,  $60^\circ$  and  $80^\circ$  respectively. The trend of increasing Balmer line emission with inclination can be seen. In RW Tri strong single-peaked emission in the Balmer lines is seen even in eclipse, indicating that the lines may be formed in a spatially extensive disc wind, and there is even a suggestion of a (potentially wind-formed) recombination continuum in the eclipsed spectrum. I have attempted to show each spectrum over a similar dynamic range.

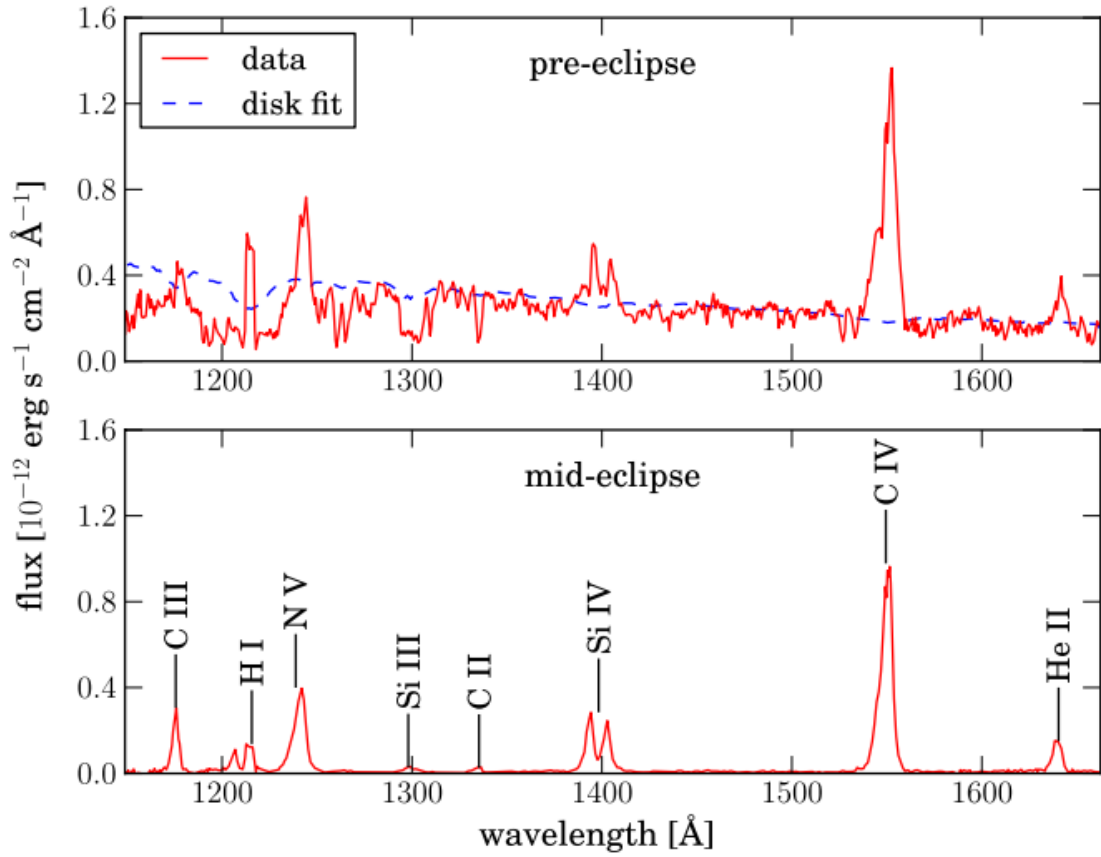


FIGURE 1.11: Credit: Noebauer et al. 2010. UV spectrum of RW Tri in and out of eclipse, showing strong lines in C IV 1550 Å and Ly $\alpha$ , among others.

close to the BH (e.g. White et al. 1988; Mitsuda et al. 1989; Uttley et al. 2014). The discovery that XRBs and CVs follow similar tracks on a hardness-intensity diagram (HID; Körding et al. 2008) is particularly interesting, especially since Ponti et al. (2012) showed that broad Fe absorption lines are only seen in the soft-state high-inclination systems (see section ??). This implies that equatorial outflows may be intrinsic to the accretion process. Although the outflow driving mechanism is probably different to CVs (e.g. Díaz Trigo & Boirin 2015), the general structure of LMXBs – that of a disc around a compact object with an associated outflow – is strikingly similar to models for CVs and quasars.

### 1.3 Quasars and Active Galactic Nuclei

Spectra of AGN have now been studied for over 100 years, and we have known that they exhibit strong, broad emission lines since the first spectrum was taken by Fath (1909). However, it wasn't until the work of Seyfert (1943) that the systematic classification

of AGN really began, leading to the phrase ‘Seyfert galaxy’. This label was applied to galaxies possessing a bright nucleus, spectroscopically characterised by a blue continuum and a series of strong emission lines. The first real physical insight into the extraordinary nature of AGN was provided by [Woltjer \(1959\)](#), who noted that (i) the nuclei must have sizes  $< 100$  pc, based on the fact that they were unresolved, and (ii) the mass of the nucleus must be very high, based on virial estimates. While both of these observations were based on simple arguments, the fact that these ultra-luminous celestial objects are both *compact* and *supermassive* is perhaps the defining insight into the nature of AGN.

Although the study of AGN was established in the optical waveband, radio astronomy also significantly furthered our understanding of AGN in the mid-20th century. A number of surveys, such as the Cambridge ([Edge et al. 1959](#)), Parkes ([Ekers 1969](#)) and Ohio ([Ehman et al. 1970](#)) surveys discovered a great many bright radio point sources distributed isotropically across the sky. These sources eventually became known as ‘quasi-stellar radio sources’, or *quasars*, and were soon found to be coincident with bright optical sources or ‘quasi-stellar objects’ (QSOs) at high redshifts ([Schmidt 1963, 1965a,b](#)). Nowadays, the term quasar normally has very little to do with radio emission and is often used interchangeably with QSO. Indeed, throughout this thesis I shall use the term quasar simply to mean a bright, massive AGN; with a sufficiently high luminosity to dominate the emission from its host galaxy.

One of the main classification schemes for AGN is a spectroscopic one, based on whether an object possesses broad emission lines in its spectrum, such as C IV, H $\beta$  and Ly $\alpha$ , in addition to the narrow lines that are always present. If these broad lines are seen, then the AGN is classed as type 1; if not, it is classed as type 2 ([Fig. 1.12](#)). These designations were originally applied to Seyfert galaxies ([Seyfert 1943](#)), but can also be used to classify the more luminous quasar class, despite the apparent difficulty in finding the expected number of type 2 quasars ([Zakamska et al. 2003](#)). This classification scheme is complicated somewhat by the existence of two unusual types of AGN: narrow line Seyfert 1s (NLS1s), which may be explained by super-Eddington accretion ([Done & Jin 2015](#)) or perhaps simply an orientation effect ([Baldi et al. 2016](#)), and so-called ‘true type 2’ AGN, in which the broad line region is absent ([Tran 2001; Shi et al. 2010](#)) rather than obscured (see next section). Despite this muddying of the waters, what was originally a clear dichotomy in spectral type provided a profound motivation for attempting to *unify* AGN via geometric arguments.

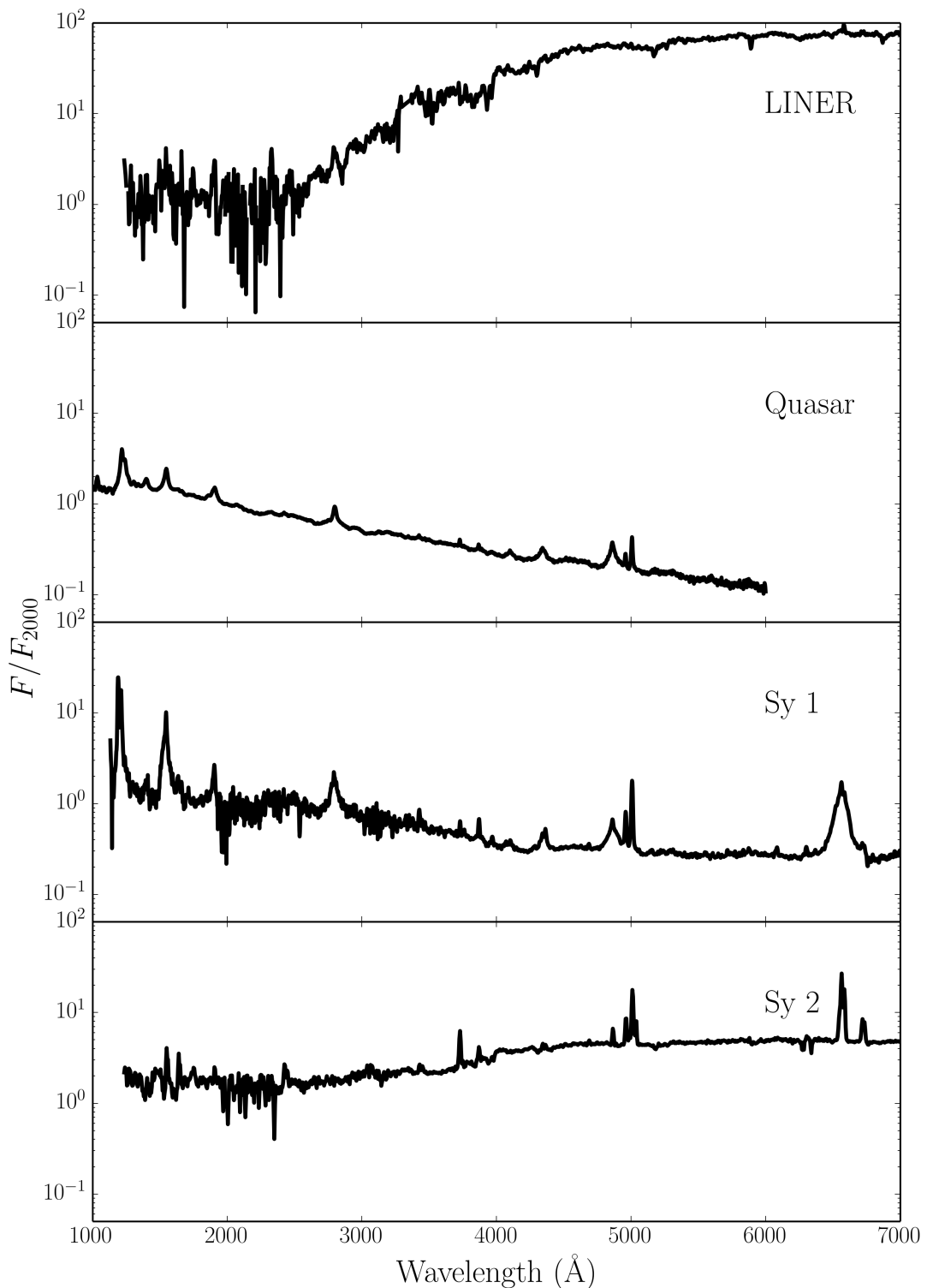


FIGURE 1.12: Template spectra, from the AGN atlas, for four common types of AGN.  
Obtained from [http://www.stsci.edu/hst/observatory/crds/cdbs\\_agn.html](http://www.stsci.edu/hst/observatory/crds/cdbs_agn.html).

### 1.3.1 AGN Unification and the Dusty Torus

Although Seyfert had identified type 1 and 2 AGN, a physical explanation for this dichotomy was not forthcoming until a study by [Antonucci & Miller \(1985, AM85\)](#). They showed unambiguously that the nearby Seyfert 2 NGC 1068 is simply an obscured type 1 AGN, by finding that broad emission lines appeared in the spectrum of *polarised* flux. This provided the basis for the first successful attempt to unify AGN behaviour, as it elegantly explained the apparent disconnect between the two types of AGN as simply a viewing angle effect: in type 1s, an observer can look directly into the broad line region (BLR) near the nucleus, but, in type 2s, this region is hidden from view. Narrow lines are seen in both types as they are formed in the narrow-line region (NLR), which is on a significantly larger scale and is thus always visible. The obscuring structure became known as the ‘torus’ ([Krolik & Begelman 1986](#)), due to its proposed geometry, and it was soon realised that this structure may be made of dust, in which case it could also be responsible for the infra-red (IR) bump in AGN spectra ([Neugebauer et al. 1979](#)).

[Urry & Padovani \(1995, UP95\)](#) went further than the original unification model proposed by AM85, as they also tried to account for the dichotomy in AGN radio properties (radio-loud/radio-quiet). The picture they proposed is shown in Fig. 1.13. This model attempts to explain all types of AGN solely in terms of viewing angle and presence, or absence, of a radio jet. Models such as this also describe the series of ‘bumps’ observed in AGN – the portions of the spectrum that dominate the luminosity, shown in Fig. 1.14. In most models, the ‘Big Blue Bump (BBB)’ is ascribed to thermal emission from an accretion disc, and the ‘Small Blue Bump’ to optically thin Balmer continuum and Fe II emission from the BLR. The latter can just be seen between  $\sim 2000 \text{ \AA}$  and  $\sim 4000 \text{ \AA}$  in the Seyfert 1 and quasar templates in Fig. 1.12. Our understanding of the BBB is still unsatisfactory (see section 1.4).

Since the seminal works by AM85 and UP95, the picture has become somewhat more complicated. Variable X-ray absorption has been detected in so-called ‘changing look’ AGN ([Matt et al. 2003; Puccetti et al. 2007](#)), including even NGC 1068 itself ([Marinucci et al. 2016](#)). Changes in type have also been seen in the optical lines; the broad H $\beta$  component in some AGN can dramatically disappear or reappear (e.g. [Tohline & Osterbrock 1976; Cohen et al. 1986; Denney et al. 2014](#)). The explanation for this could be variable absorption ([Elitzur 2012](#)) or a change in the accretion state of the disc. In the latter case, it has even been suggested that a disc wind could be directly responsible

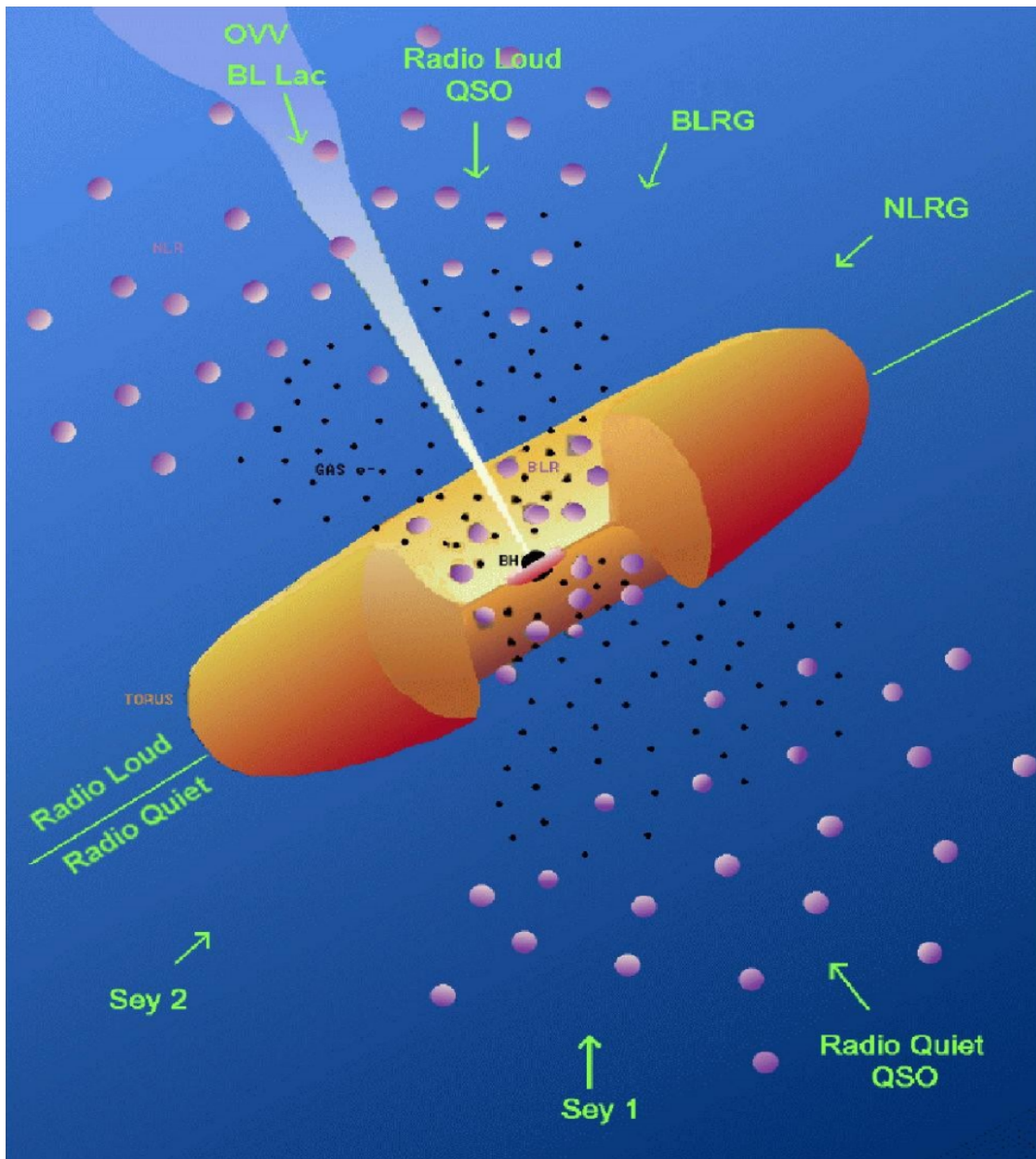


FIGURE 1.13: A unified scheme for AGN. The broad line region is compact and can thus be obscured from view by a dusty torus, whereas the larger narrow line region is always visible. The radio-loud/radio-quiet dichotomy is explained by the presence or absence of a radio jet.

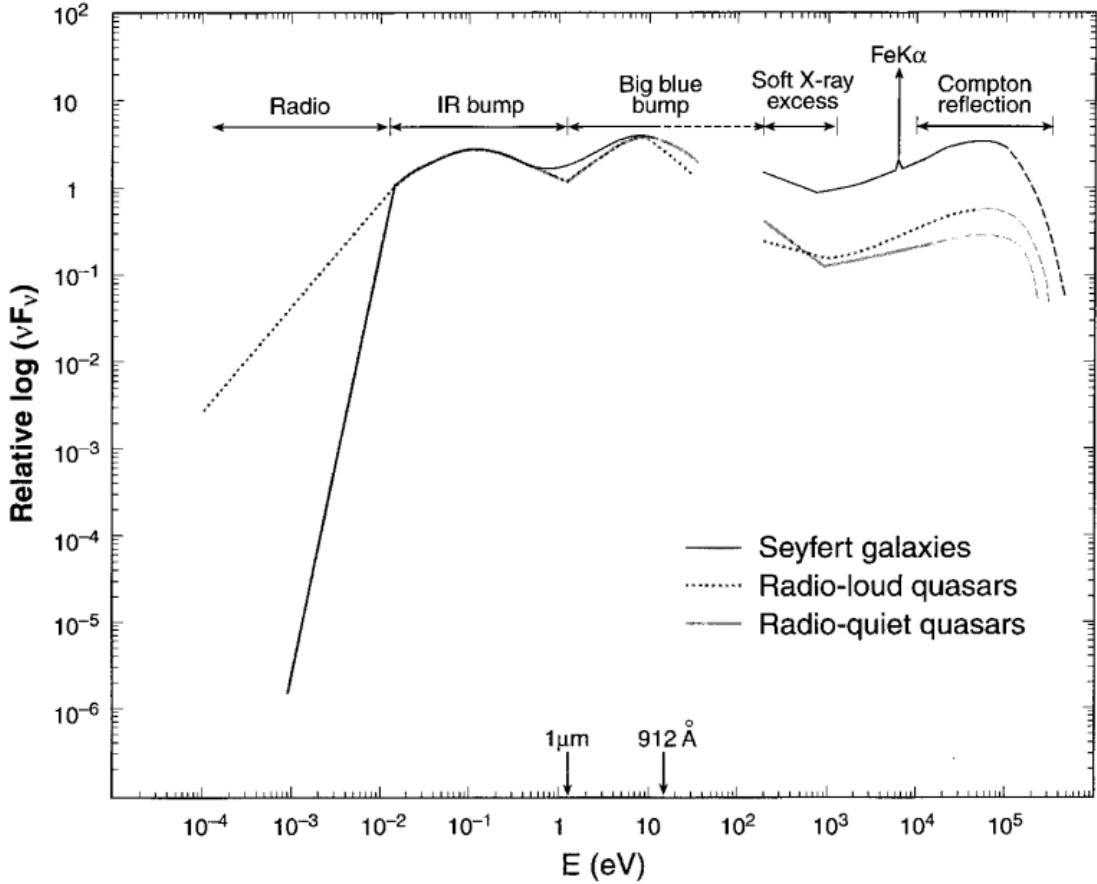


FIGURE 1.14: Credit: Koratkar & Blaes 1999 Approximate average broadband SEDs for a few types of AGN. The series of characteristic bumps can be clearly seen. The Soft-X-ray excess is also visible (see section 1.3.2.1).

for this switch (Elitzur et al. 2014). Furthermore, dusty *polar* outflows have been found to be important IR emitters (Hönig et al. 2013), implying that, even when it comes to dust, the torus is not the whole picture. Despite these complications, the AGN torus unification picture still explains a lot of AGN phenomenology and represents a useful framework that can be tested with observations.

### 1.3.2 X-ray Properties of AGN

Approximately 10% of the bolometric luminosity of AGN comes out in the X-ray band, between  $\approx 0.1$  and  $\approx 100$  keV. Thus, AGN dominate the cosmic X-ray background (Madau et al. 1994). The hard X-ray emission typically follows a power law shape with spectral index -0.9 (e.g. Koratkar & Blaes 1999), widely considered, as in LMXBs, to come from a hot ‘corona’ of electrons close to the BH that upscatters disc seed photons (e.g. Haardt & Maraschi 1991). The compactness of this X-ray corona has been confirmed by microlensing (Chartas et al. 2009; Dai et al. 2010) and variability studies

(Green et al. 1993; Crenshaw et al. 1996; Risaliti et al. 2007; Emmanoulopoulos et al. 2014). Indeed, X-rays in AGN can be highly variable, both in terms of their intrinsic X-ray emission, but also due to changes in the absorption characteristics (Risaliti et al. 2002; Miller et al. 2008; Connolly et al. 2014). I discuss X-ray absorption in more detail in chapter 2, particularly with respect to disc winds.

The hard X-ray spectra of AGN also tend to exhibit a number of reflection features. Typically, these consist of a strong Fe K $\alpha$  emission line and a ‘Compton hump’ at high energies. The latter is produced by Compton down-scattering of high energy photons (Pounds et al. 1989; Nandra & Pounds 1994). It is still unclear exactly where these features originate, but a common interpretation is that they are caused by reflection off the inner parts of the accretion disc (Fabian et al. 1995; Iwasawa et al. 1996a; Reynolds 1999). If this is the case, and the broadening of the iron line is relativistic, this would allow for measurements of the BH spin (Laor 1991; Iwasawa et al. 1996b; Dabrowski et al. 1997). This hypothesis is somewhat controversial, as many of the relativistic features supposedly imprinted by BH spin can also be explained by Comptonisation or absorption (e.g. Misra & Kembhavi 1998; Miller & Turner 2013). In addition, an outflow can naturally produce the characteristic broad red Fe K $\alpha$  wing (Sim et al. 2010).

In Compton-thick AGN, the intrinsic continuum is heavily absorbed by columns of  $N_H \gtrsim 10^{24} \text{ cm}^{-2}$  – this absorption is normally attributed to the dusty torus, but disc winds could also contribute. Compton-thick AGN are required in large numbers in order to explain the cosmic X-ray background (Setti & Woltjer 1989). In these sources, reflection features can actually dominate the X-ray spectrum (Alexander et al. 2011; Gandhi et al. 2013), but the Fe line is formed from low ionization stages of Fe on  $\sim 0.1 \text{ pc}$  scales (Gandhi et al. 2015).

### 1.3.2.1 The Soft X-ray Excess

If one interpolates between the  $\nu^{1/3}$  law from the BBB in the UV, and the power law in the hard X-rays, a curious excess of flux is often found in type 1 AGN (see Fig. 1.14, and Koratkar & Blaes 1999). This is known as the soft X-ray excess (SXXS), which is too hot to be explained by thermal disc emission, as a thin disc around an AGN should never approach the temperatures required. Many models have been proposed to explain this excess, including relativistically smeared photoabsorption (Gierliński & Done 2004,

2006), relativistically smeared line and free-free emission (Ross & Fabian 2005; Crummy et al. 2006) and a variety of cool Comptonised component geometries, such as an inner accretion flow (Magdziarz et al. 1998; Done et al. 2012) or a geometrically thin layer on top of the disc (Janiuk et al. 2001). While the SXSS poses a challenge to the simplest pictures of AGN, it may also solve some of the outstanding puzzles, since some of the geometries proposed may help to explain the accretion disc size problem discussed in section 1.4 (Gardner & Done 2016).

### 1.3.3 The Broad Line Region: Connection to Winds and Unification

In the UP95 unification model, the broad emission lines come from a series of virialised clouds close to the disc plane. As noted by Murray et al. (1995, hereafter MCGV95), there are a number of problems with the BLR ‘cloud’ model, perhaps most notably that there is no obvious physical origin for such virialised clouds. Testing alternative models for the BLR is therefore important. Indeed, MCGV95 proposed a disc wind model in order to explain both BALs and BELs in quasars. A disc wind model was also discussed by Elvis (2000), who proposed a structure for quasars that attempted to explain much of the behaviour of luminous AGN merely as a function of viewing angle. It is worth noting that there is observational support for the unification paradigm; for example, it has been suggested that orientation is a key driver of the so-called ‘Eigenvector 1’ relationship in quasars (Boroson & Green 1992; Sulentic et al. 2000; Marziani et al. 2001; Shen & Ho 2014). Disc wind unification models are discussed further in section 2. The philosophy of these models is that, before invoking additional degrees of freedom in a model, we should first test if known quasar phenomenology (disc winds) can explain other aspects of their observational appearance. I have illustrated this general principle with the ‘Occam’s quasar’ cartoon shown in Fig. 1.15. This is the picture that I will quantitatively test in the latter, quasar-focused sections of this thesis. The same general principle can also be applied to cataclysmic variables and other accreting objects.

## 1.4 The Current Understanding of the Disc Continuum

The SS73 model is still the most common way to fit accretion disc spectra and infer information about the underlying physics. However, a number of issues have been raised concerning the thin-disc model and its applicability to accreting systems.

OCCAM'S QUASAR: THE PRINCIPLE THAT IN EXPLAINING A QUASAR NO MORE ASSUMPTIONS SHOULD BE MADE THAN ARE NECESSARY.

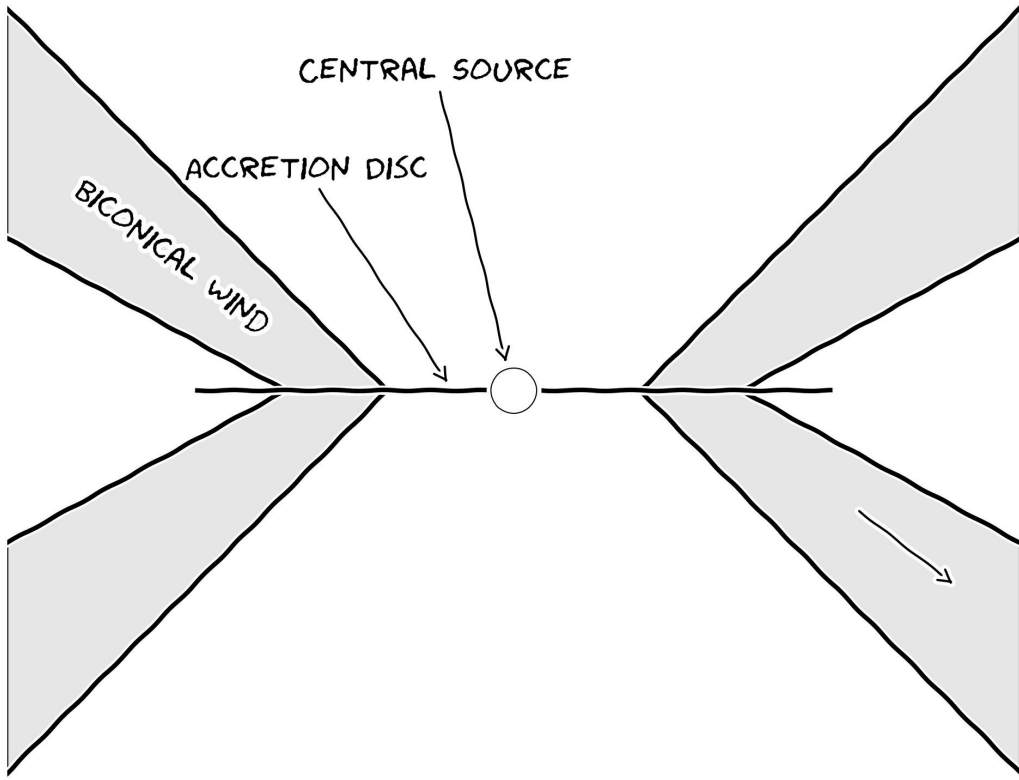


FIGURE 1.15: Occam's quasar. How far can this general picture take us when trying to explain the behaviour of quasars and other accreting compact objects?

#### 1.4.1 The Spectral Shape of CV Discs

Attempts to fit the observed SEDs of high-state CVs with simple disc models have met with mixed success. In particular, the SEDs predicted by most stellar/disc atmosphere models are too blue in the UV (Wade 1988; Long et al. 1991, 1994; Knigge et al. 1998a) and exhibit stronger-than-observed Balmer jumps in absorption (Wade 1984; Haug 1987; La Dous 1989; Knigge et al. 1998a). One possible explanation for these problems is that these models fail to capture all of the relevant physics. Indeed, it has been argued that a self-consistent treatment can produce better agreement with observational data (e.g. Shaviv et al. 1991; but see also Idan et al. 2010). However, an alternative explanation, suggested by Knigge et al. (1998b; see also Hassall et al. 1985), is that recombination continuum emission from the base of the disc wind might fill in the disc's Balmer absorption edge and flatten the UV spectrum.

Alternatively, it may just be that CV disks are never really in a steady state, and so we should only expect the  $R^{-3/4}$  temperature profile to hold in a limited portion of the disc. From eclipse mapping, it has been shown that the inferred accretion rate increases with radius in NLs (Rutten et al. 1992; Horne 1993). These results suggest that a non-radiative form of energy loss is present in the inner regions of the disc, of which potential forms may be advection or mass loss. This is yet another piece of evidence that the understanding of accretion and outflow are intertwined, although hopefully not inextricably.

### 1.4.2 The Big Blue Bump in AGN

Does the SS73 model apply well to AGN spectra? There are contrasting views on the matter. On the one hand, Antonucci (2013) claims that “most of the AGN community is mesmerized by unphysical models that have no predictive power”. Yet a recent spectral fitting study by Capellupo et al. (2015) concludes that “altogether, these results indicate that thin accretion discs are indeed the main power houses of AGN”. So, what are the main problems when confronting thin disc models with observation?

#### 1.4.2.1 The Accretion Disc Size Problem

One of the most interesting results of recent years relating to AGN and accretion discs is the discovery that the continuum emission region size appears to be a factor  $\sim 3$  larger than predicted by standard thin disc theory. This result has been found independently in both microlensing (Morgan et al. 2010; Dai et al. 2010) and reverberation (Edelson et al. 2015) studies, and poses a challenge to the current best-fit model for the big blue bump in AGN. One proposed solution is that the discs in AGN are inhomogeneous, consisting of individual clumps with independently varying temperatures (Dexter & Agol 2011), but this is very much still an active area of research. It is worth noting that the impact of winds on these results has not yet been properly quantified, something our team is currently trying to address (Mangham et al. 2016).

#### 1.4.2.2 Fitting AGN Spectra and the 1000 Å Break

AGN spectra do not, in general, exhibit the canonical  $\nu^{1/3}$  slope (e.g. Koratkar & Blaes 1999; Davis et al. 2007; Shankar et al. 2016) or colour-mass scalings (Bonning et al. 2007)

expected from theoretical predictions. Furthermore, there is a characteristic break in AGN spectra at around 1000 Å ([Lusso et al. 2015](#)), which does not scale with BH mass or luminosity, as one might expect for a break associated with an accretion disc. There is also no evidence in AGN of the expected polarisation signatures from an optically thick disc atmosphere ([Stockman et al. 1979](#); [Antonucci 1988](#); [Antonucci et al. 1996](#)).

Despite these problems, recent work suggests that the thin disc model still has some potential. [Capellupo et al. \(2015\)](#) were able to fit a number of AGN spectra in the UV and optical with thin disc models, although successful fits were only found once they included effects such as Comptonisation and mass loss, as well as correcting for extinction. BH spin also had a reasonable effect on the spectral fits, although it is somewhat difficult to constrain from spectral fitting alone. The 1000 Å break has also been explained with mass-losing discs ([Laor & Davis 2014](#)), and [Lusso et al. \(2015\)](#) suggested that incorrect IGM corrections may be exacerbating the effect. So, while many problems exist, it may not be time to abandon the good ship “Shakura-Sunyaev” just yet.

## 1.5 The Universality of Accretion

Accretion appears to be an important physical processes across  $\sim 10$  orders of magnitude in mass. But is this process the same on all scales? Does any behaviour manifest in all accreting systems?

### 1.5.1 The RMS-flux relation

Broad-band variability is common in all types of accretion disc. It has been known for some time that there exists a linear relationship between the flux and absolute root-mean-square (rms) amplitude of this variability. This was discovered first in XRBs and AGN ([Uttley & McHardy 2001](#); [Uttley et al. 2005](#); [Heil et al. 2012](#)), but it has been shown more recently that the relationship extends to CVs and even YSOs ([Scaringi et al. 2012, 2015](#)). The relationship is also not limited to just one type of CV but is present in both NLs and DNe ([Van de Sande et al. 2015](#)).

The model that best reproduces this behaviour is the so-called ‘fluctuating accretion disc’ model ([Lyubarskii 1997](#); [Kotov et al. 2001](#); [Arévalo & Uttley 2006](#); [Hogg & Reynolds](#)

(2015). More generally, additive processes cannot reproduce this behaviour, and a multiplicative mechanism is required (Uttley et al. 2005). Regardless of the mechanism, the rms-flux relation is one of the most clear-cut examples of a universal accretion phenomenon. It tells us that at least some of the behaviour in CV discs is also present in AGN and XRBs, strengthening the argument that CVs can be used as ‘accretion laboratories’.

### 1.5.2 Accretion states and disc-jet coupling

Variable and transient sources are common in astrophysics, particularly when the sources are accreting. It turns out that when one plots the colour and luminosity evolution over the course of an outburst cycle it follows very similar tracks in both CVs and XRBs (see Fig. 1.16, Körding et al. 2008). This colour-luminosity behaviour traces the accretion state of the system. The detection of radio jets is intrinsically linked to this accretion state (disc-jet coupling), as jets only appear in the ‘hard’ accretion state, to the right of the so-called ‘jet line’ (Fender 2001; Fender et al. 2004). Körding et al. (2008) showed that this behaviour also occurs in CVs, as radio emission in the DN SS Cyg is detected in the same region of colour-luminosity space. In addition, there is a well-known correlation between radio and X-ray luminosities in low-hard states (Gallo et al. 2003).

Clear connections between disc state and radio loudness have also been found in AGN. Perhaps the most obvious piece of evidence that disc-jet coupling is scale invariant is the so-called ‘fundamental plane of BH activity’ (Merloni et al. 2003), which extends from LMXBs right up to quasars. AGN have been shown to occupy similar regions of colour-luminosity space to the LMXBs (Körding et al. 2006), and simulations involving scaled-up LMXB discs have been successful in reproducing AGN accretion states (Sobolewska et al. 2011). Correlations in X-ray photon index are present in AGN and LMXBs; ‘softer when brighter’ behaviour is found at relatively high Eddington ratios (McHardy et al. 1999; Gu & Cao 2009), while ‘harder when brighter’ is observed in low states (Gu & Cao 2009; Emmanoulopoulos et al. 2012; Connolly et al. 2016).

Despite this apparently universal behaviour, the jet production mechanism in BHs is not well known. Theoretical work suggests that radio jets should be correlated with BH spin (Penrose & Floyd 1971; Blandford & Znajek 1977), but whether such a correlation exists in LMXBs is controversial (Fender et al. 2010; Narayan & McClintock 2012). This has

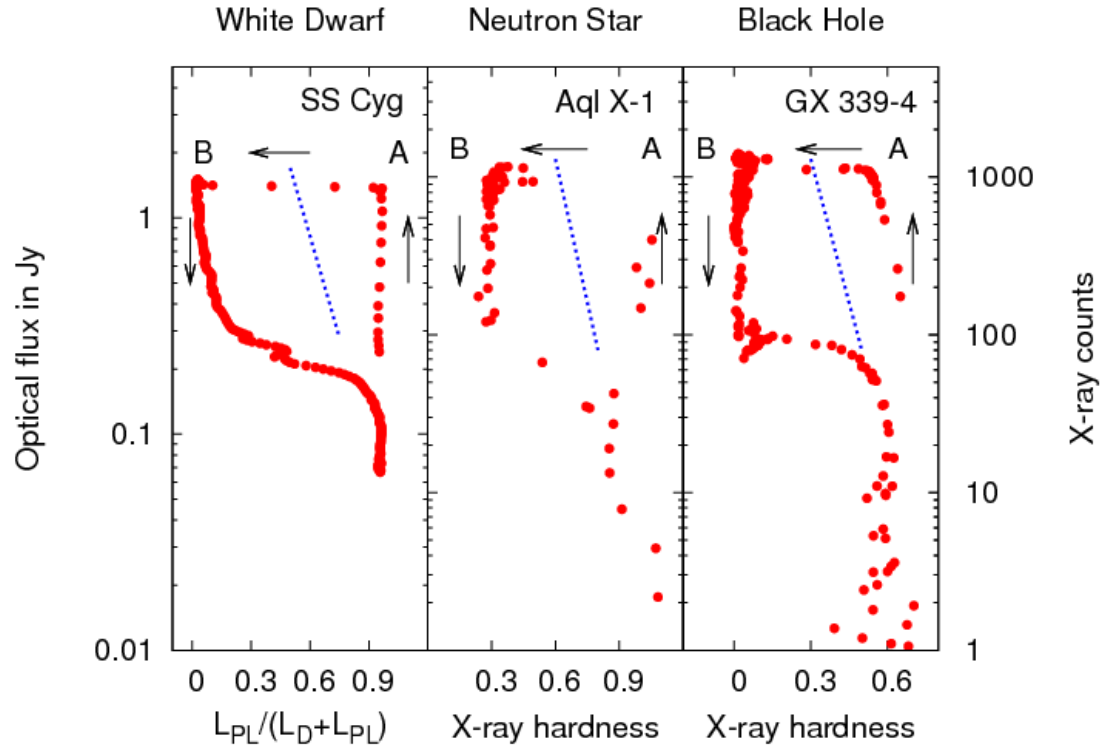


FIGURE 1.16: Credit: Kording et al. 2008. Caption.

significant implications for AGN; if powerful radio jets are associated exclusively with rotating BHs then the number of radio-loud AGN would imply a large fraction of them must be rapidly spinning, with high radiative efficiencies. Further evidence that radio jets are not simply produced by RIAFs onto spinning BHs is found when one considers that NLs show evidence of synchrotron radio emission ([Coppejans et al. 2015](#)). This important result suggests that our understanding of jets is incomplete, and that the links between accretion state and jet production are fundamental, but unsolved. Disc winds may complicate, or simplify, matters, depending on one's outlook (see chapter 2).

### 1.5.3 A Global Picture

Clearly, accretion physics is relevant to a plethora of astrophysical phenomena, and at least some of the physics of accretion is applicable to *all* classes of accreting object. It would also appear that the outflowing material observed in accreting systems has a profound effect on the accretion process itself, and possibly significantly affects the observational appearance of disc-accreting systems (c.f. Elvis' unification model). Hence, in the next chapter, I will review the evidence for winds and discuss some of the relevant background theory.

## Chapter 2

# Quasar Emission Lines as Probes of Orientation and Unification

*This chapter is based on a paper in preparation:*

*Matthews J. H., Knigge C., ‘Quasar Emission Lines as Probes of Orientation and Unification’, to be submitted to MNRAS.*

### 2.1 Introduction

In the previous chapter, I presented tests of geometric unification models using MCRT and photoionization simulations. One of the key results from that analysis is that trends with inclination prohibit models with equatorial outflows matching observations, as the EWs of the broad emission lines tend to increase with inclination. This conclusion is strongly dependent on the outflow geometry and suggests that understanding the orientations of BALQSOs, or, equivalently, the opening angles of their winds, is crucially important if we are to establish the validity of geometric unification models. The motivation to measure orientations is not limited to disc wind models; the AM85 and UP95 unification schemes described in section 1.3.1 both attempt to explain the diverse behaviour of AGN merely as a function of viewing angle. Orientation indicators therefore also allow us to explore if these models adequately explain the type 1/type 2 dichotomy in AGN. Furthermore, constraining outflow geometries is not only important for unification. The covering factor and opening angle of the outflow are important quantities for

estimating the feedback efficiency (e.g. [Borguet et al. 2012](#)), measuring the BAL fraction (e.g. [Krolik & Voit 1998](#)) and understanding the outflow physics (e.g. [Proga 2005](#)).

Unlike in galactic accretion disc systems, measuring inclinations for quasars and AGN is notoriously difficult. Obtaining reliable orientation indicators is thus an important observational goal for the community (see e.g. [Marin 2016](#)). Perhaps as a result of this problem, directly opposing geometries have been proposed for BAL outflows (see section ??). Attempts to constrain the inclinations of BALQSOs have been made previously with different diagnostics; for example, by considering radio measurements ([Zhou et al. 2006](#); [DiPompeo et al. 2012b](#)), polarisation ([Brotherton et al. 2006](#)) and emission line properties ([DiPompeo et al. 2012a](#)).

One potential way to estimate quasar inclination is by comparing the emergent flux of a roughly isotropic emission line to the continuum, which is expected to be strongly anisotropic if it is emitted from a geometrically thin, optically thick accretion disc. It follows that, if we can estimate the angular distribution of line and continuum emission, the EW of an emission line can act as an orientation indicator. Conversely, if the orientations of quasars were well-known then the emission line EW distribution could be used to test models for the origin of the UV and optical continuum. The variation of EW with inclination is demonstrated neatly by the behaviour of emission lines in high-state CVs, where inclinations are fairly well constrained. High-state CVs show a clear trend of increasing line EW with inclination ([Hessman et al. 1984](#); [Patterson 1984](#); [Echevarria 1988](#); [Noebauer et al. 2010](#), see also sections ?? and ??), a trend that is attributed to foreshortening of the disc continuum.

The ideal emission line to use for this method would be one that is completely isotropic, i.e. *optically thin*. The [O III] 5007 Å narrow emission line is a strong, forbidden line formed in the narrow-line region (NLR) of AGN, and should thus be completely isotropic. Any dispersion in the distribution of [O III] 5007 Å EW (EW[O III]) must therefore be driven by some combination of the intrinsic luminosity ([Boroson & Green 1992](#)) the covering factor/geometry of the NLR ([Baskin & Laor 2005](#)) and the inclination of the system. In a recent study, [Risaliti et al. \(2011\)](#) showed that the EW[O III] distribution could be well-fitted by a simple model driven purely by disc inclination. In this chapter, I apply a similar method in order to provide a fundamental test of BAL and non-BAL quasar unification models in which the continuum source is a geomtrically thin, optically thick disc. This is motivated by the remarkably similar emission line properties of BAL

and non-BAL quasars – a similarity that would not be expected from the simplest models in which BALQSOs are viewed from equatorial angles.

This chapter is structured as follows. First, I describe the data sample and selection criteria being used. I begin by simply examining the distributions of the EW of the [O III] 5007 Å emission line, EW[O III], and comparing the BAL and non-BAL quasar distributions. In section 2.3, I review the angular distribution of continuum emission one would expect from simple  $\alpha$ -disc models, as well as exploring more advanced disc models computed with AGNSPEC. I then use these theoretical angular distributions applied to a simple toy model in section 2.4, and conduct MC simulations in an attempt to fit the observed LoBAL and non-BAL quasar distributions of EW[O III], using a similar approach to Risaliti et al. (2011). In section 2.5, I discuss the results in the context of radio and polarisation measurements of AGN, and explore the location of BAL quasars in ‘Eigenvector 1’ parameter space. I also consider the broad emission line distribution in HiBAL quasars in more detail. Finally, in section 2.6, I summarise the results.

## 2.2 Data Sample

The data sample is based upon the Shen et al. (2011, hereafter S11) catalog of 105,783 quasars from the The Sloan Digital Sky Survey (SDSS) Data Release 7 (DR7). As I will use emission line diagnostics in this study, this sample must be further divided according to which emission lines are present in the SDSS wavelength range at a given redshift. Sample A contains all quasars within the redshift range  $0.35 < z < 0.83$ , such that the Mg II 2800 Å and [O III] 5007 Å line EWs are both measured, and Mg II BAL identification is possible. Sample B contains all quasars within the redshift range  $1.45 < z < 2.28$ , such that the EWs and presence of BAL in Mg II 2800 Å and C IV 1550 Å are both measurable. The details of these samples are shown in table 1. The mass and Eddington fraction measurements from S11 of the two samples, are shown in Fig. 2.1 against the background distribution of all S11 quasars.

S11 are careful to take into account traditional problems with quasar line fitting, such as narrow line or Fe pseudocontinuum contamination, in their fits to emission line profiles and resultant EW measurements. For Mg II 2800 Å this includes careful subtraction of the Fe emission using the Vestergaard & Wilkes (2001) templates. This subtraction is not included for C IV 1550 Å, as the Fe emission is less prominent and harder to model.

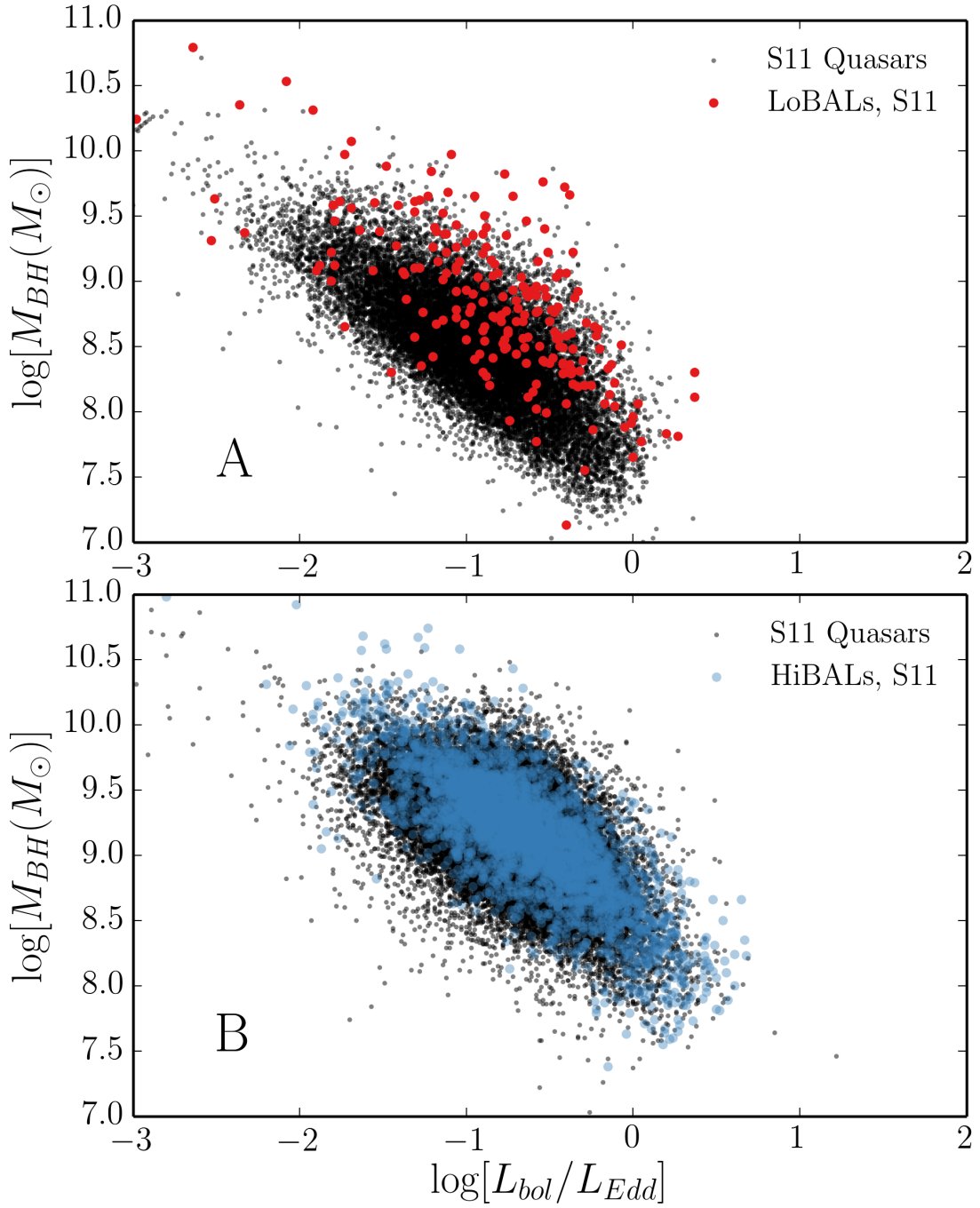


FIGURE 2.1: BH mass and Eddington fraction measurements from S11 for Sample A (top) and Sample B (bottom). The LoBALs in sample A and BALs in Sample B are also plotted in each case.

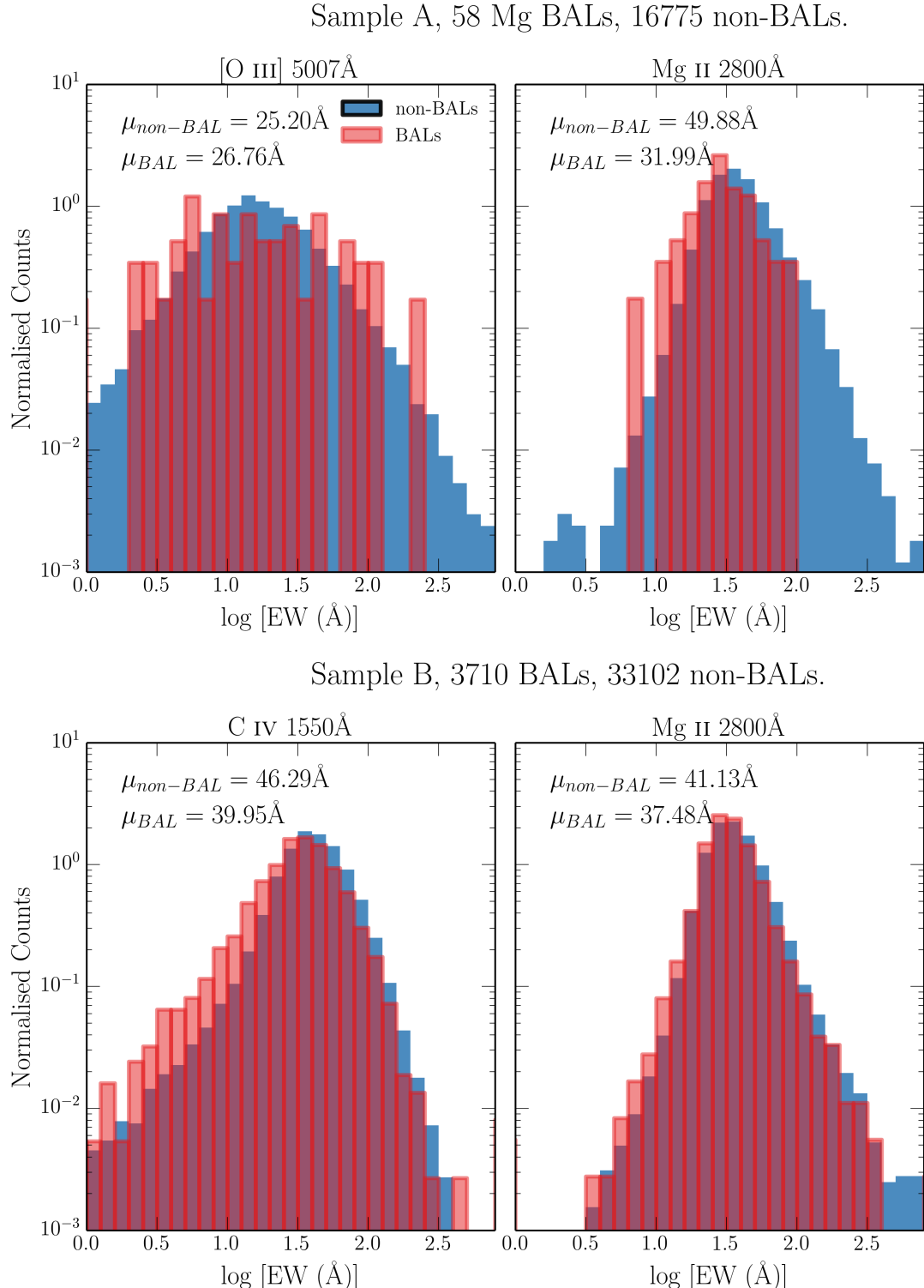


FIGURE 2.2: Histograms of equivalent widths for three emission lines from the two different samples. The mean of the BAL and non-BAL quasar distributions are labeled in each case, and the histograms are normalised so that they integrate to 1.

This may lead to a systematic overestimate by  $\sim 0.05$  dex in the C IV line EW. The [O III] 5007 Å line is fitted with a Gaussian. The flux ratio of this line with the sister component of the doublet, [O III] 4959 Å, is found to agree well with the theoretical expectation of around 3, implying a reliable subtraction of broad H $\beta$ . In order to mask out the effects of e.g., absorption, on the C IV and Mg II lines, S11 ignore  $3\sigma$  outliers in the fit to the profile. Based on these considerations, the S11 catalog makes for a reliable set of EW measurements. This is especially true when making inferences from multiple emission lines, as systematics inherent to individual lines or spectral windows are less likely to affect the analysis as a whole.

In attempting to draw broad conclusions about unification models as a whole, I would ideally construct a large, homogenous dataset of *HiBAL* and non-BAL quasars, both with [O III] 5007 Å EWs. Unfortunately, the wavelength limits of SDSS do not allow this, and only LoBAL quasars have both BALs and EW[O III] measurements. One of the problems with using just LoBAL quasars in tests of unification is that there is evidence that they are drawn from a different population than normal quasars. Examples include anomalously high LoBAL fractions in dust-reddened quasar samples ([Urrutia et al. 2009](#)) and infra-red selected samples ([Dai et al. 2012](#)); although see also [Lazarova et al. \(2012\)](#).

Fig. 2 shows histograms of a number of different emission line properties for samples A and B. As discussed by previous authors (e.g. [Weymann et al. 1991](#)), I find that BAL and non-BAL quasars seem to possess very similar emission line properties. The EW is related to the intrinsic, ‘face-on’ equivalent width,  $\text{EW}_*$  by the equation

$$\text{EW} = \text{EW}_*/\epsilon(\theta) \quad (2.1)$$

where  $\theta$  is the viewing angle with respect to the symmetry axis and  $\epsilon(\theta)$  is the ‘angular emissivity function’, which describes how the continuum luminosity from the disc varies as a function of viewing angle. For a foreshortened disc this is simply  $\epsilon(\theta) = \cos \theta$ . Note that this assumes isotropic line emission, but the effect of line anisotropy is discussed in section 2.5.4.

Thus, if BALQSOs are preferentially viewed from larger-than-average viewing angles, we would expect them to possess higher EWs. We might also expect that the distribution of EWs is broader in this case due to the shape of a  $\cos \theta$  curve. It is already apparent from Fig. 2.2 that the BALQSO distribution means are not significantly higher than the

non-BAL quasar means – in fact, in many cases they are lower. This is not expected from a model in which the continuum comes from a foreshortened disc, and BAL outflows are at all equatorial. This problem is examined further in section 2.4. First, I will examine the motivations for different forms of  $\epsilon(\theta)$  in AGN and quasars.

## 2.3 The Angular Distribution of Emission from an Accretion Disc

As introduced in chapter 1, the most widely-used theoretical model for accretion discs is the so-called ‘ $\alpha$ -disc’ model of SS73. There are a number of well-documented problems when fitting AGN SEDs with SS73 accretion disc models (see section 1.4). Despite these problems, Capellupo et al. (2015) succeeded fitting  $\alpha$ -disc models to AGN spectra when the effects of GR, mass-loss and comptonisation were included. In this section, I start by discussing the angular distribution of emission from a classic SS73 disc, before exploring opacity and GR effects. In order to do so, I use AGNSPEC (Hubeny et al. 2000; Davis & Hubeny 2006; Davis et al. 2007). I stress that the discussion here is not limited to  $\alpha$ -discs; the only real condition for the angular distributions derived here is that the disc is geometrically thin and optically thick.

### 2.3.1 Standard Thin Disc Models

Any geometrically thin, optically thick disc will appear foreshortened and limb darkened (if temperature decreases with height from the central disc plane). Foreshortening is a simple  $\cos \theta$  geometric effect, where  $\theta$  is the inclination with respect to the vertical  $z$  axis, which is perpendicular to the disc plane. Limb darkening,  $\eta(\theta)$ , is usually approximated by a linear dependence of the emergent flux on  $\cos \theta$ , i.e.

$$\eta(\theta) = a(1 + b \cos \theta), \quad (2.2)$$

where  $a$  is a normalisation constant, and  $b$  governs the strength of the limb darkening. Setting  $b = 3/2$ , known as the Eddington approximation, tends to give good agreement with solar observations (e.g. Mihalas 1978). The two effects can be combined to give a

net angular emissivity function of

$$\epsilon(\theta) = a \cos \theta \left( 1 + \frac{3}{2} \cos \theta \right). \quad (2.3)$$

### 2.3.2 Including GR and Opacity Effects

In reality, limb darkening is not frequency independent and depends on the bound-free and bound-bound opacities in the disc. In addition, it has been shown that GR light bending can ‘isotropize’ the radiation field in XRBs (Zhang et al. 1997; Muñoz-Darias et al. 2013), in some cases overcoming foreshortening effects. In order to assess the impact of GR and disc opacities on  $\epsilon(\theta)$ , I use AGNSPEC models, which conducts a stellar atmosphere calculation to obtain the SED from a series of annuli, before using the KERRTRANS code to calculate the emergent SED by ray-tracing along Kerr geodesics. Fig. 2.3 shows  $\epsilon(\theta)$  as a function of  $\theta$  for two AGNSPEC models for minimally and maximally spinning BHs. The models are characterised by  $M_{BH} = 10^9 M_\odot$  and an Eddington fraction of 0.2. The angular distribution is fairly insensitive to these choices. For comparison, I also show foreshortened and limb-darkened predictions for SS73 models. Although the AGNSPEC continua are significantly more isotropic at 500 Å, there is very little effect redward of around 1000 Å, which is the relevant region of  $\epsilon(\theta)$  for [O III] 5007 Å, C IV 1550 Å and Mg II 2800 Å. In fact, using the foreshortened estimate is the conservative (least anisotropic) prescription in these regimes. I will thus adopt  $\epsilon(\theta) = \cos \theta$  for the remainder of this work.

## 2.4 Predicted EW Distributions Compared to Observations

### 2.4.1 Fitting the Quasar Distribution

Risaliti et al. (2011, hereafter R11) analysed the EW[O III] distribution of 6029 quasars in SDSS DR5. They demonstrated that a foreshortened disc and isotropic [O III] 5007 Å line produces a high EW tail in the EW distribution, with a characteristic slope of  $\Gamma_{EW} = -3.5$ . In order to first reproduce their result and discuss its implications, I have created a sample according to their selection criteria. The criteria are that the object in question lies in the redshift range 0.01 to 0.8, have an absolute magnitude  $M_i > 22$ , an

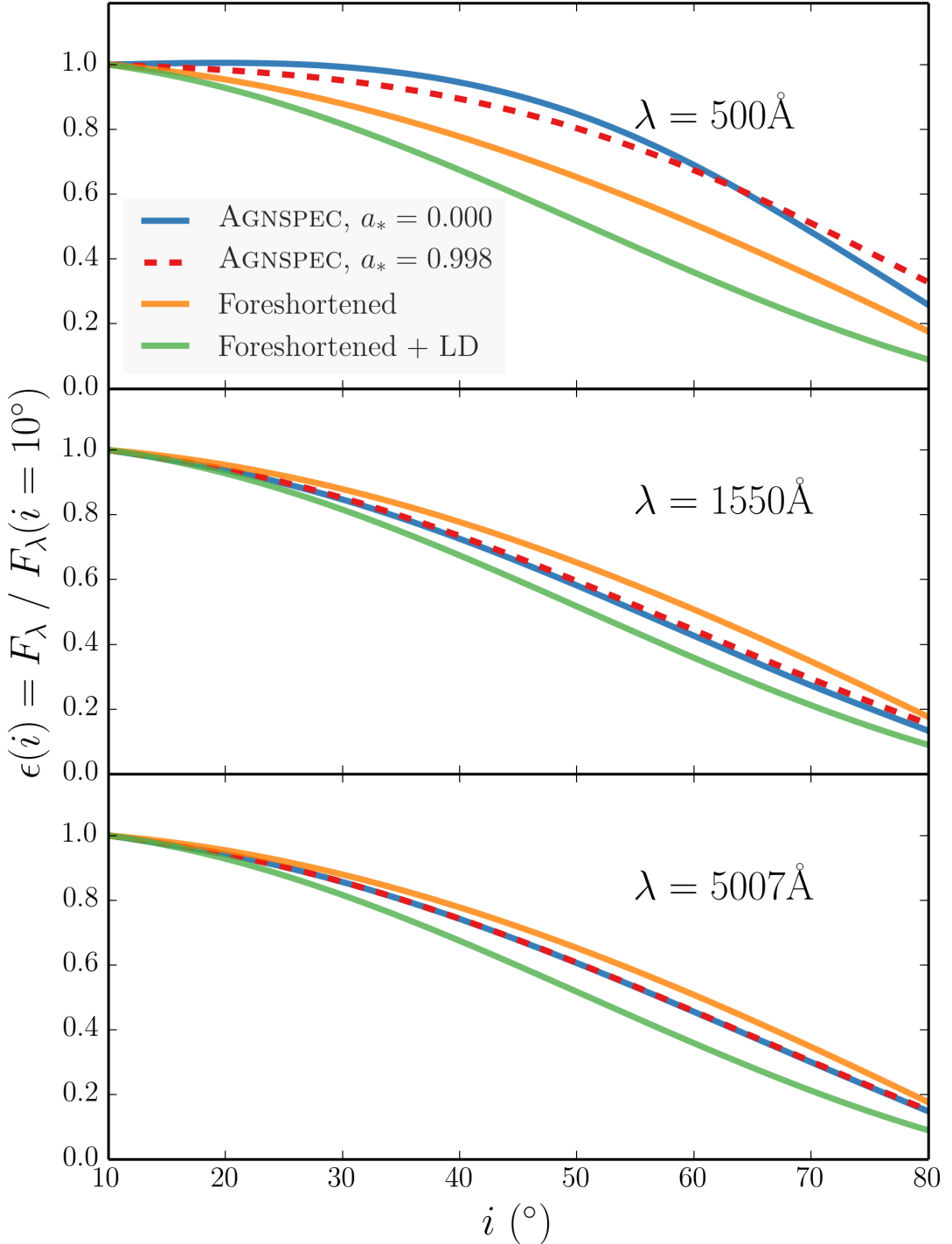


FIGURE 2.3: Angular variation of continuum luminosity from AGNSPEC and classical thin disc models. The monochromatic continuum luminosities is divided by the monochromatic continuum luminosity at  $10^\circ$ , from AGNSPEC and classical thin disc models, at three different wavelengths. The models are computed for an Eddington fraction of 0.2 and  $M_{BH} = 10^9 M_\odot$ . In each panel I show both Kerr and Schwarzschild AGNSPEC models, and the classical models are for both pure foreshortened discs and foreshortened and limb darkened (LD) discs.

apparent magnitude  $m_i > 19.1$ , and signal to noise per pixel of greater than 5. Using the updated SDSS quasar sample of S11, this defines a sample of 14,424 quasars.

To fit the distribution, I conduct the following procedure, which is similar to the method R11 use to demonstrate that the power law tail is expected.

1. A set of isotropic angles is chosen such that  $P(\theta) \propto d\Omega(\theta)$ . If  $\theta < \theta_1$  then the fake object is designated as unobscured, and otherwise the object is ignored.
2. To be included in the sample, the object also has to survive a selection test to simulate the distribution of angles in a flux-limited sample. This is done by drawing a random sample from the real quasar sample, and calculating a ‘doubly observed continuum flux’,  $F_O$  at 5100Å (rest frame), such that  $F_O = F_{5100} \epsilon(\theta)$ . The flux limit is set at  $5 \times 10^{-13}$  erg s<sup>-1</sup> cm<sup>-1</sup> Å<sup>-1</sup>, but the results are fairly insensitive to the limit chosen.
3. For each mock sample, an  $\text{EW}_*$  is drawn from an intrinsic (i.e. ‘face-on’) EW distribution for quasars. This is assumed to be a Gaussian distribution. The mean,  $\mu_*$ , and width,  $\sigma_*$ , of this Gaussian can either be set arbitrarily – for example, to demonstrate trends in mock data – or obtained from a  $\chi^2$  fit to the observed EW distribution.
4. A mock EW is estimated such that  $\text{EW} = \text{EW}_*/\epsilon(\theta)$ , and this process is repeated to build up a mock sample of  $10^6$  objects.

The result of this numerical experiment is, as found by R11, a distribution with a high EW tail of slope  $-3.5$ . I can now vary the maximum angle,  $\theta_1$ , and examine how this tail changes. Mock data for a series of maximum angles is shown in Fig. 2.4, for two different intrinsic Gaussians. The power law behaviour is only seen when the maximum angle is sufficiently large, and a rapid decay in the distribution is observed at a characteristic EW related to both the width and mean of the intrinsic distribution as well as the cosine of the maximum angle. The top panel has  $\mu_*$  and  $\sigma_*$  of the R11 Model 1, whereas the bottom panel shows a narrower distribution to illustrate the earlier onset of the high EW cutoff. In principle, this cutoff could be used to infer information about the viewing angle distribution of quasars.

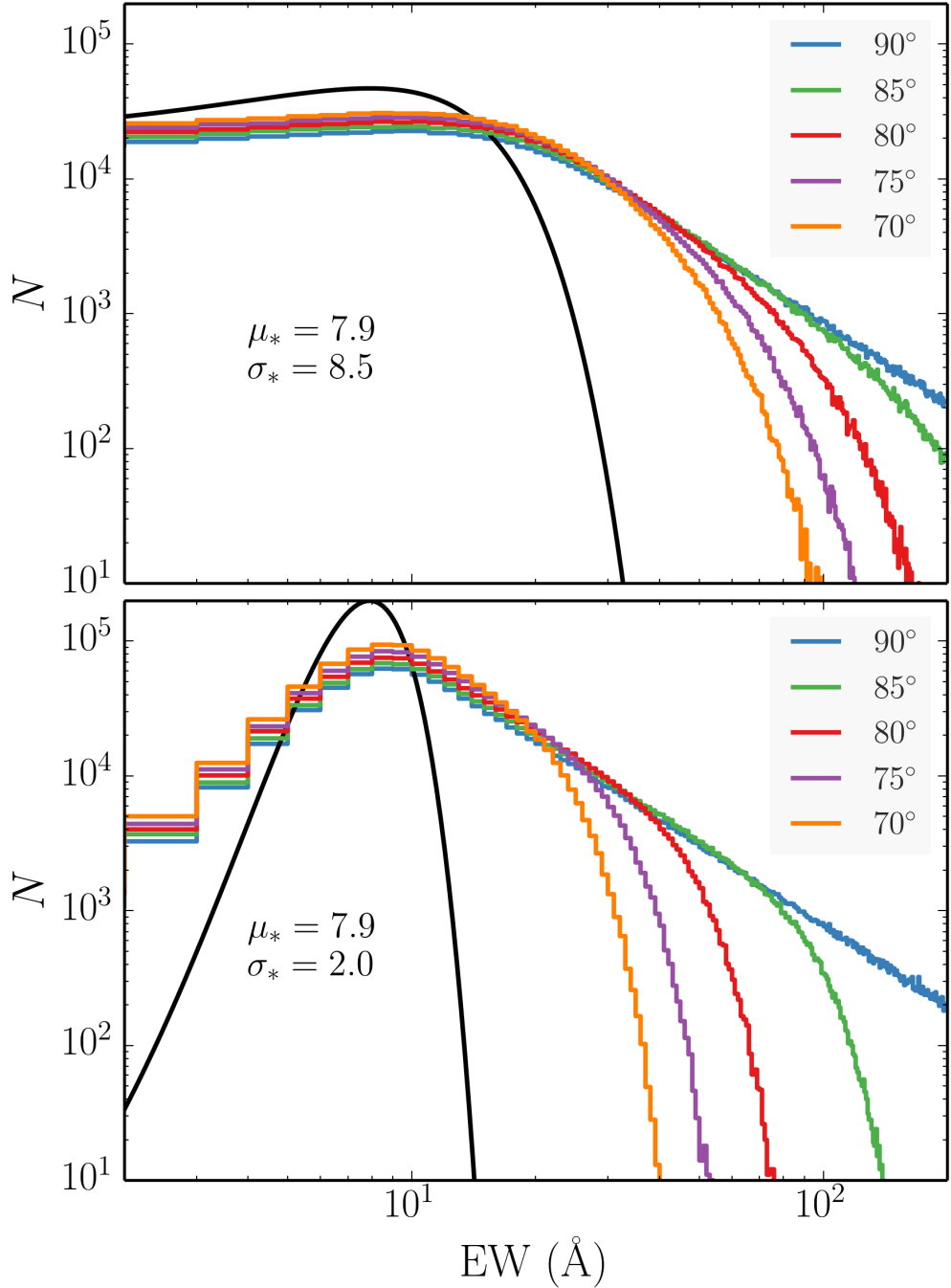


FIGURE 2.4: Theoretical EW distributions from the numerical experiment described in section 2.4.1 for a few different maximum angles. The results in the top panel use the same intrinsic distribution as Model 1 from R11 (shown in black), whereas the bottom panel shows the distributions obtained from a narrower intrinsic Gaussian. By the time the maximum angle is limited to around  $70^\circ$  the cutoff is clear even at moderate values of EW.

Fig. 2.5 shows the result of a  $\chi^2$  minimization fit to the R11 sample. The best fit is achieved with a maximum angle of  $\theta_1 = 83.5^\circ$  and a narrower intrinsic distribution than model 1 of R11. The run of  $\chi^2$  with maximum angle is shown in Fig. 2.6, where the choice for  $\mu_*$  and  $\sigma_*$  is left free in each case. Maximum angles below  $\sim 80^\circ$  are strongly disfavoured by this model. I adopt linear binning to facilitate easy comparison with R11, and only fit up  $\text{EW} = 100\text{\AA}$  due to poor statistics above that limit. This makes inferring any information about a potential high EW cutoff difficult as a more complete sample at high EW is required.

#### 2.4.2 Comparing non-BAL and LoBAL Distributions: Sample A

In order to compare the observed distributions to those expected for LoBALS and non-BALs I conduct a Monte Carlo simulation similar to the process described in section 2.4.1, but with a few key differences. I once again assume  $\epsilon(\theta) = \cos \theta$ . The geometry of the toy model used in this simulation is shown in Fig. 2.7.

First, A set of isotropic angles is generated. If  $\theta_{\min} < \theta < \theta_{\max}$  then the fake object is flagged as a mock BAL. If  $\theta < \theta_{\min}$  then the fake object is designated a non-BAL, and otherwise the object is ignored. Once again, the object also has to survive a selection test based on a arbitrary flux selection limit. I then fit the non-BAL distribution using the method described previously. For each mock sample, a  $\text{EW}_*$  is drawn from the intrinsic gaussian, and a mock EW is estimated such that  $\text{EW} = \text{EW}_*/\epsilon(\theta)$ . This process is repeated to build up a mock sample of objects, and carried out for a series of pairs of  $\theta_{\min}$  and  $\theta_{\max}$ . This allows theoretical distributions for BAL and non-BAL quasars for a series of different outflow geometries to be derived.

The diagnostics recorded from the simulation are the following four quantities:

- The  $p$ -value associated with a two-tailed Kolgomorov-Smirnov (K-S) test statistic,  $p_{KS}$ , in which the mock BAL sample is compared to the real LoBAL sample.
- The BAL fraction,  $f_{BAL}$ , is calculated from the number of objects in the mock sample with  $\theta_{\min} < \theta < \theta_{\max}$ .
- The  $\chi^2/\text{dof}$  from the fit to the non-BAL quasar distribution.
- $\Delta\mu_{EW}$ , the difference between the mean value of the mock BAL distribution and the mean value of the mock non-BAL distribution.

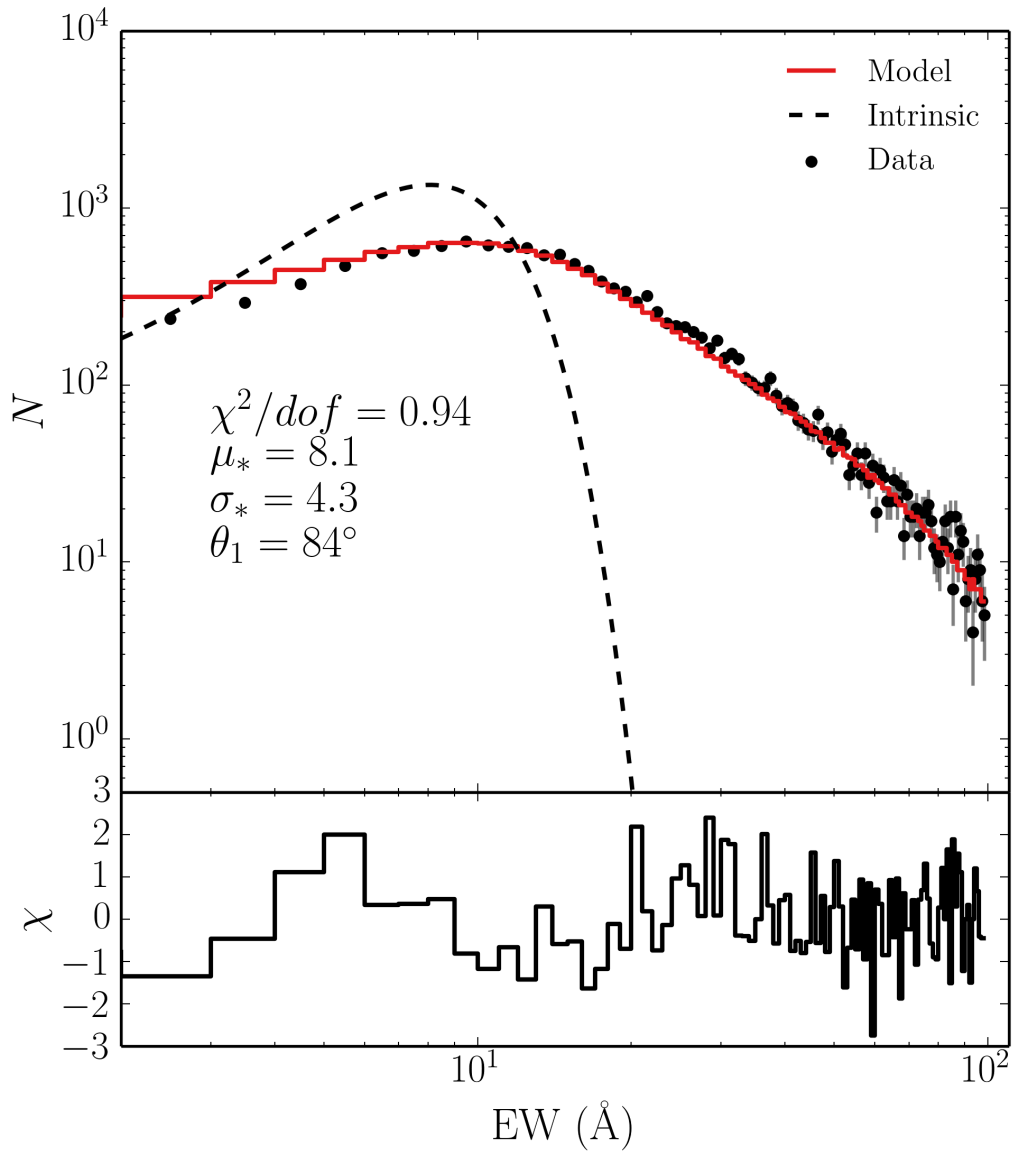


FIGURE 2.5: The EW[O III] distribution of quasars in the R11 sample (black points), with  $\sqrt{N}$  errorbars, and the best fit model with a maximum viewing angle of  $84^\circ$ . The intrinsic Gaussian distribution is shown with a dotted line. The non-BAL plot is equivalent to the non-BAL histogram in the top left panel of Fig. 2.2, except that it uses linear binning and adopts the R11 sample criteria rather than using sample A.

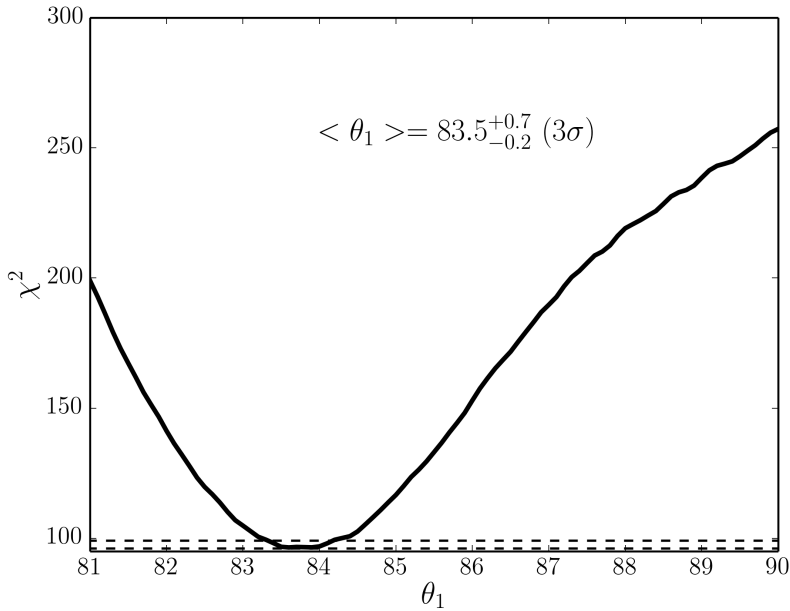


FIGURE 2.6:  $\chi^2/dof$  as a function of maximum angle,  $\theta_1$ , calculated in steps of  $0.1^\circ$ .  
The choice for  $\mu_*$  and  $\sigma_*$  is left free in each case.

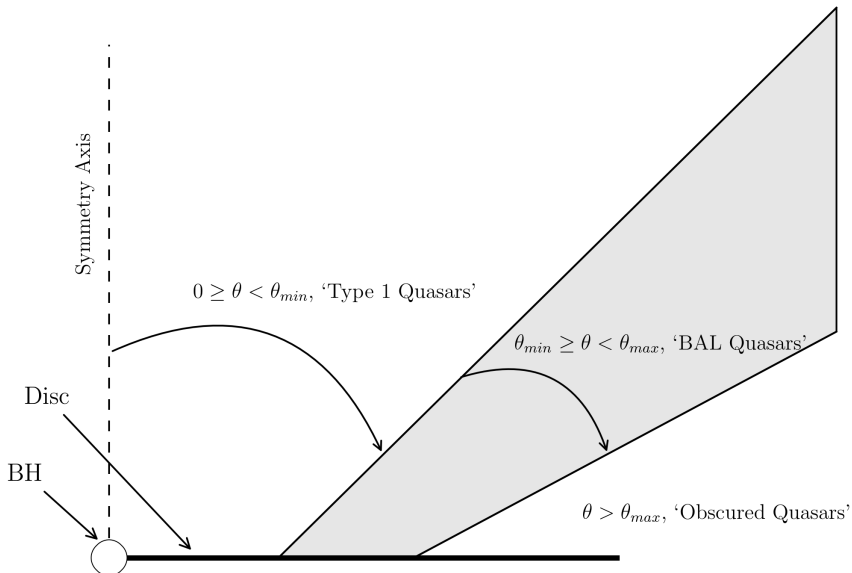


FIGURE 2.7: The geometry of the toy model used to carry out the Monte Carlo simulations.

The simulation results are shown in figure 2.8, in which the four diagnostics are plotted as a function of  $\theta_{min}$  and  $\theta_{max}$ .

As expected, equatorial viewing angles for LoBAL quasars are disfavoured, and furthermore, it is only possible to fit the tail to the EW[O III] distribution if non-BAL quasars are allowed to be viewed from high inclinations. There is no region of parameter space where a satisfactory fit is obtained to the quasar distribution without simultaneously obtaining a large value of  $\Delta\mu_{EW}$ . The K-S test allows us to reject the null hypothesis. The simulations favour a geometry in which BAL quasars are viewed from very similar angles to non-BAL quasars.

The conclusions here are limited by the lack of knowledge about the intrinsic face-on distribution of EW[O III], or equivalently, the orientations of the quasars themselves. If either of these quantities were known then the results of the K-S test and  $\chi^2$  minimization could be used to place more robust constraints on BAL and non-BAL viewing angles and the associated covering factor of the outflow. Furthermore, the distribution of C IV quasar EW cannot be fit by the same model as the EW[O III] distribution.

A key limitation is due to the SDSS wavelength coverage and means that only LoBALS can be used when EW[O III] is present (sample A). I would suggest that future observational programs might look to build up a large sample of EW[O III] measurements for HiBAL quasars.

## 2.5 Discussion

I have demonstrated that the EW distributions of the [O III] 5007 Å emission line in LoBAL and non-BAL quasars is not consistent with a model in which LoBAL quasars are viewed from equatorial angles and the continuum emission originates from a foreshortened accretion disc. The EW distributions of C IV 1550 Å suggest that a similar conclusion applies to HiBAL quasars. This result would only be strengthened were I to include limb darkening. I will now explore how the above results compare to other observations of quasars that might probe system orientation, as well as the potential impact of obscuration and line anisotropy on the results.

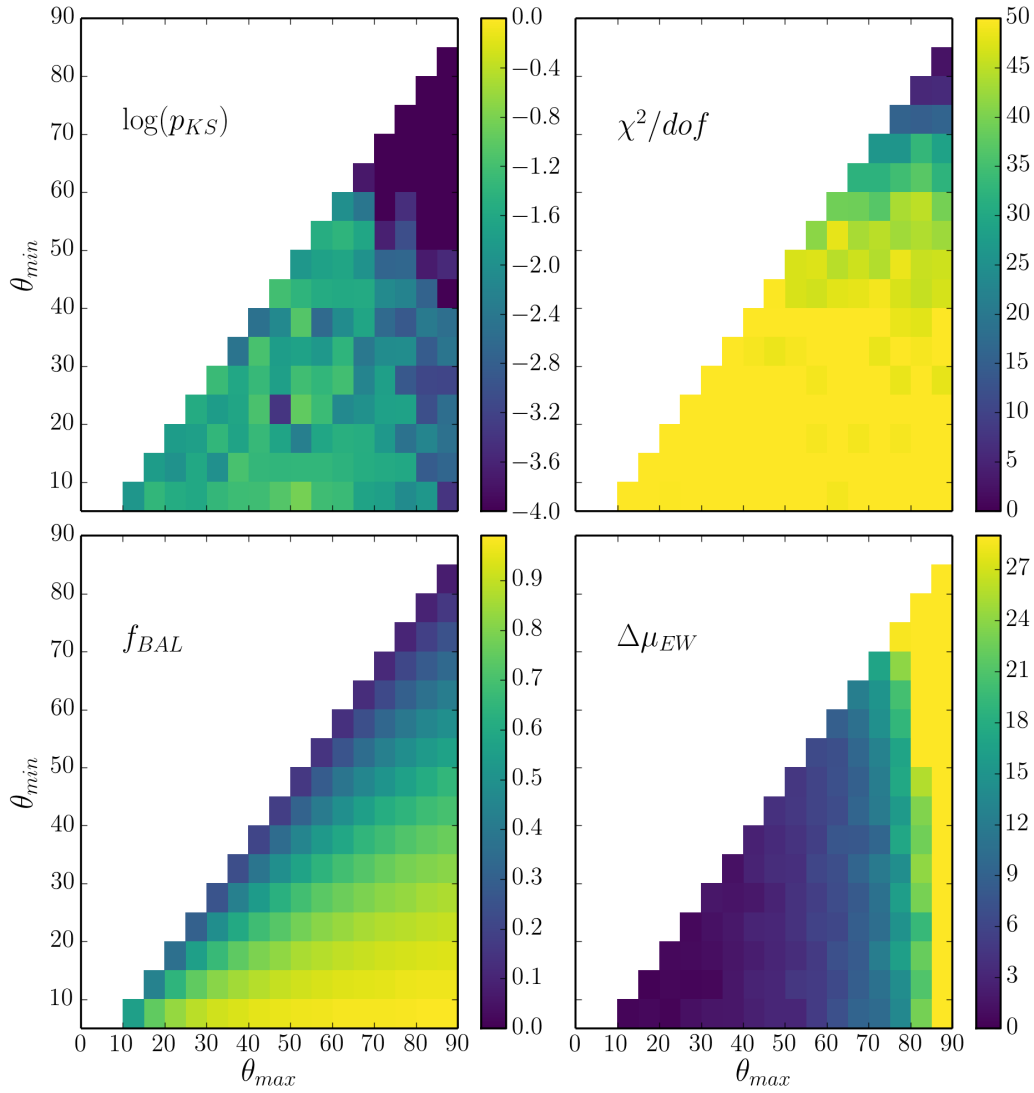


FIGURE 2.8: Heat map showing the results of the MC simulation described in section 2.4.2. The quantities shown are discussed further in the text, but correspond to (clockwise from top left): the  $p_{KS}$  value from a comparison between the mock BAL dataset and the observed BAL dataset, the reduced  $\chi^2$  from the fit to the non-BAL EW distribution, the difference in mean EW between the mock BAL and mock non-BAL datasets, and the BAL fraction expected for the geometry in question.

### 2.5.1 Eigenvector 1

Eigenvector 1 (EV1) is a fundamental parameter space for AGN and quasars (Boroson & Green 1992; Sulentic et al. 2000; Marziani et al. 2001; Shen & Ho 2014). It relates the FWHM of H $\beta$ , the relative iron strength,  $R_{\text{FeII}}$ , and EW[O III]. Both EW[O III] and FWHM[H $\beta$ ] have been used as orientation indicators, and so comparing the LoBALQSO EV1 distribution to the non-BAL quasar EV1 distribution is particularly interesting. Once again, HiBALs cannot be placed on this space due to the lack of rest-frame optical coverage.

Fig. 2.9 shows the quasar distribution from sample A in EV1 parameter space, with LoBAL quasars from sample A overplotted. [Shen & Ho \(2014, hereafter SH14\)](#) propose that the main inclination driver in this parameter space is FWHM[H $\beta$ ], and that high inclination sources should thus cluster around a diagonal line from the lower right to upper left quadrants. In contrast, R11’s analysis predicts that high inclination sources should cluster around high EW OIII widths. As EW[O III] and FWHM[H $\beta$ ] are very weakly correlated (Spearman’s rank coefficient of 0.14), this means they should lie to the left of the parameter space. Inspection of the figure clearly shows that BAL quasars are not only found in one region of the EV1 parameter space.

In order to assess this more quantitatively, I also show contours of quasar counts overlaid on the scatter plot. The contours correspond to the number of objects in each bin, where the bins are of size  $\Delta R_{\text{FeII}} = 0.2$  and  $\Delta \text{FWHM}[\text{H}\beta] = 500 \text{ km s}^{-1}$ . The percentage of quasars falling within the inner contour is 45%, whereas only 18% of LoBALQSOs fall in the space. Conversely, 24% of LoBALQSOs fall outside the outermost contour compared to 10% of non-BAL quasars. It would therefore appear that BAL quasars are preferentially clustered towards the high-mass and high-inclination end of EV1 space (under the interpretation of SH14). This is further illustrated by Fig. 2.11, which shows the LoBAL fraction in larger bins, compared to the mean LoBAL fraction. This is again suggestive of an overdensity of LoBALQSOs towards the upper right of the parameter space. It is also clear that a unification picture in which BAL quasars are viewed exclusively from high inclinations is inconsistent both the R11 and SH14 interpretations.

Larger datasets, preferably including HiBAL quasars with EV1 measurements, are needed in order to properly constrain the EV1 behaviour of BAL quasars. However, overall, the behaviour of EV1 in LoBALQSOs slightly strengthens the conclusion that BAL quasars are not always viewed from extreme inclinations.

### 2.5.2 Polarisation

Spectropolarimetry of BAL quasars offer some of the best insights into the geometries of BAL outflows and tends to show a few key properties. The first is enhanced polarisation in the BAL troughs themselves ([Schmidt & Hines 1999](#)). This is readily explained by a scattering region unobscured by the BAL trough, with the higher polarisation percentage simply due to the decreased direct flux. This may also explain the non-black saturation in BAL troughs (see section ??).

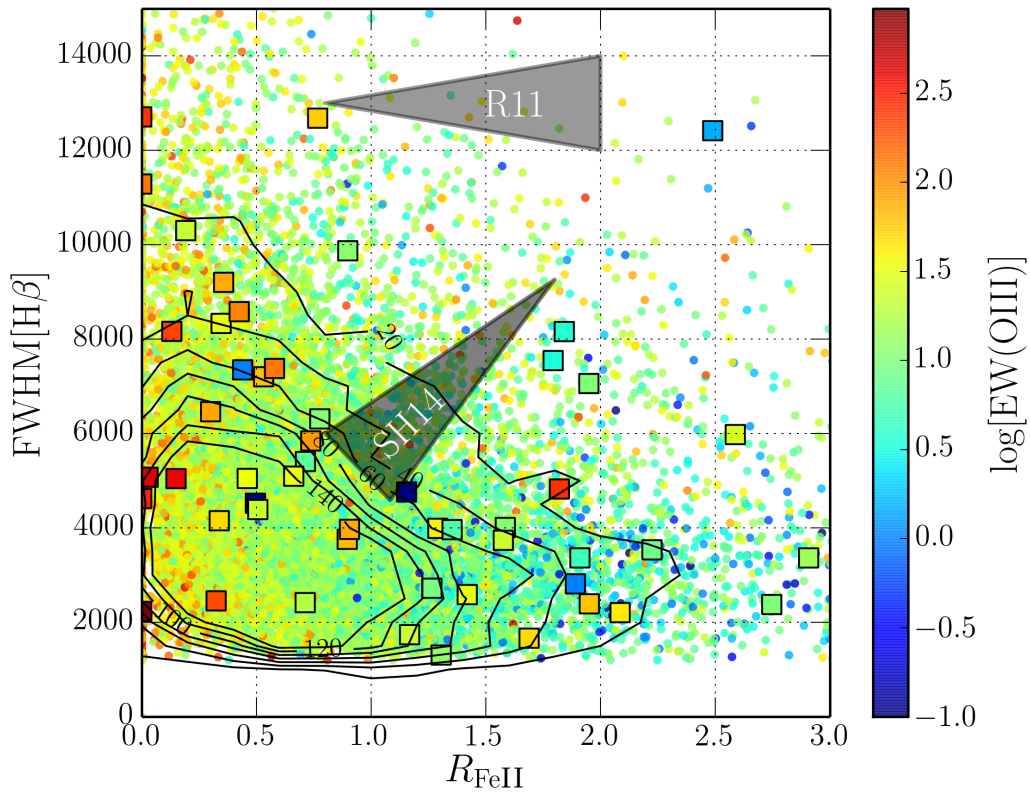


FIGURE 2.9: Eigenvector 1 for BAL and non-BAL quasars. FWHM of the H $\beta$  line plotted against the relative iron strength,  $R_{\text{FeII}}$ . The colour coding corresponds to the EW of OIII. The dots mark all quasars from sample A, while the squares mark those with Mg II BALs. The shaded triangles show the approximate direction of the expected inclination trend under the SH14 and R11 interpretations.

The second property is a continuum polarisation percentage that is around 2.4 times greater, on average, than seen in the non-BAL population (Schmidt & Hines 1999). A histogram of the continuum polarisation percentages of a sample of BAL quasars from Schmidt & Hines (1999) are compared to the Type I and Type II AGN populations from Marin (2014) in Fig. 2.12. The corresponding cumulative distribution function is shown in Fig. 2.13. These show that BAL polarisation percentages seem to lie between those of type 1 and type 2 AGN. If type 1 and type 2 objects are viewed from low and high inclinations, respectively, as expected from unified models and suggested by Marin (2014, 2016), this would imply an intermediate inclination for BALQSOs. This enhanced polarisation for BALQSOs, relative to non-BAL systems, is also well reproduced by intermediate inclination outflows in simple radiative transfer models (Marin & Goosmann 2013).

The third characteristic polarisation property of BALQSOs is a polarisation angle of  $\gtrsim 60^\circ$  with respect to the radio jet axis in RL objects (Brotherton et al. 2006, and

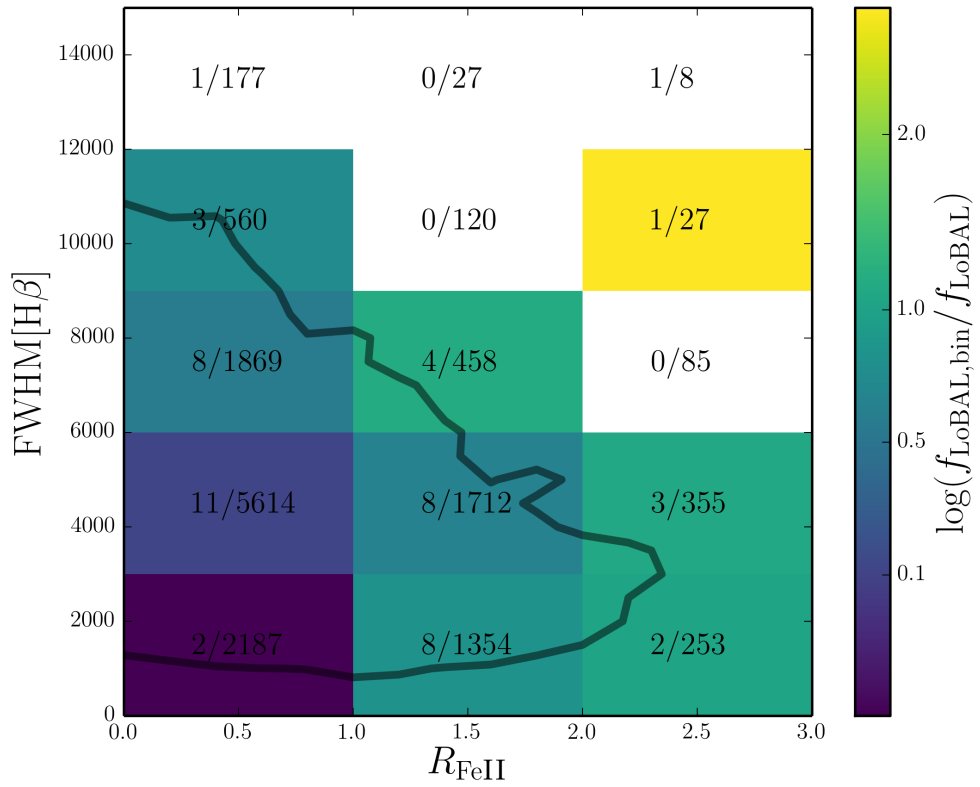


FIGURE 2.10: LoBAL fraction compared to global LoBAL fraction in Eigenvector 1 space, in bins of  $\Delta R_{\text{FeII}} = 1$  and  $\Delta \text{FWHM}[\text{H}\beta] = 3000 \text{ km s}^{-1}$ . The contour shows the outermost contour from Fig. 2.9 for reference. The text shows  $N_{\text{LoBAL}}/N_{\text{non-BAL}}$ , where  $N_{\text{LoBAL}}$  is the number of LoBALQSOs in the bin and  $N_{\text{non-BAL}}$  in the number of non-BAL quasars in the bin.

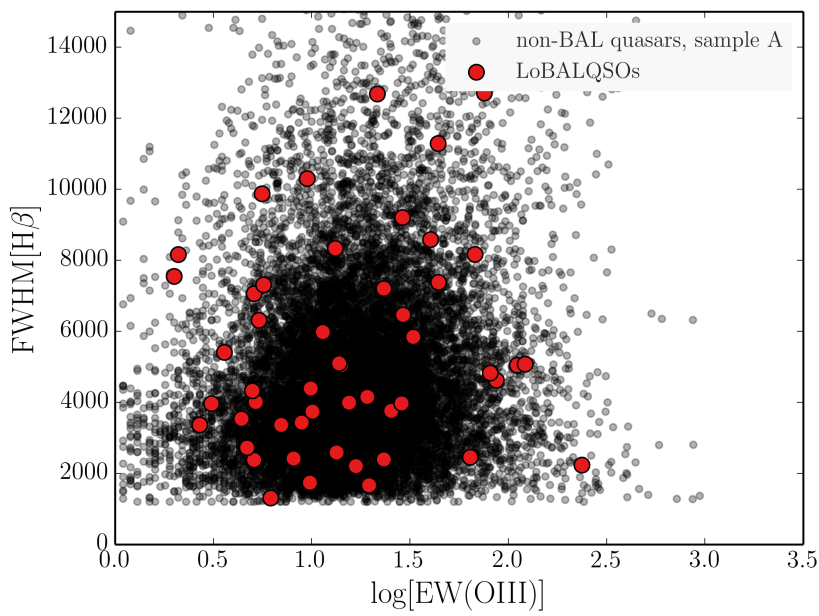


FIGURE 2.11: FWHM BLAH

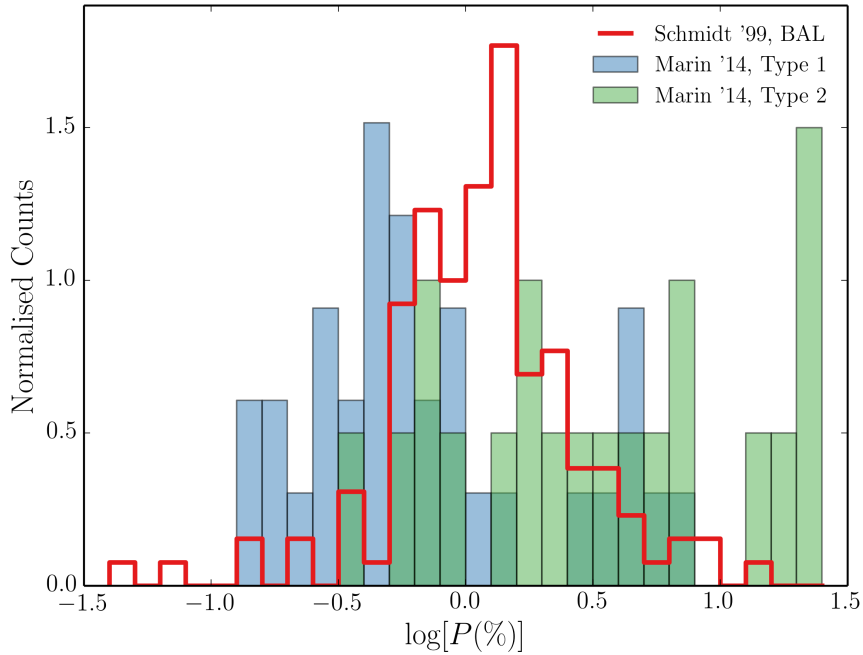


FIGURE 2.12: Histograms of polarisation percentages for BAL quasars from Schmidt et al. (1999) together with the Marin et al. (2014) AGN sample.

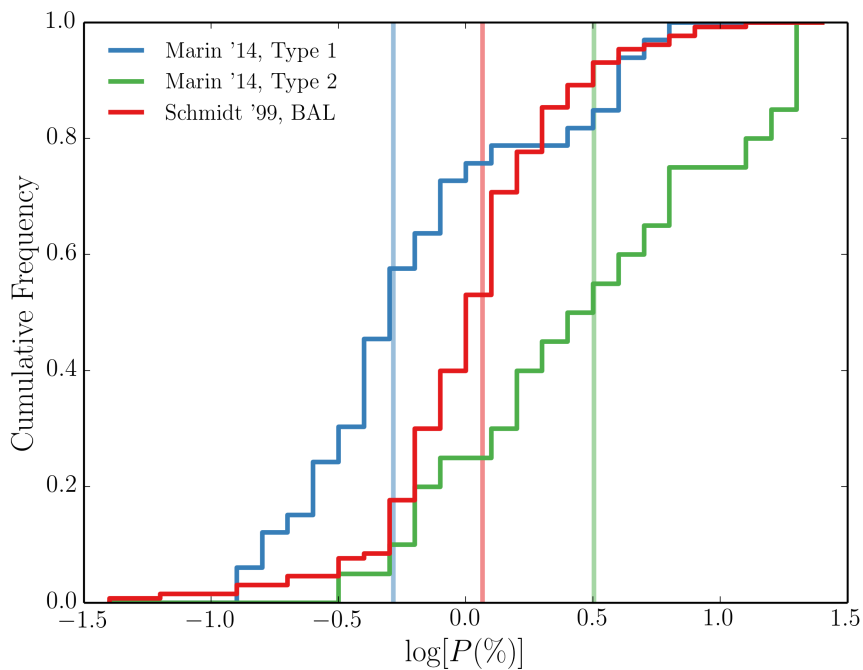


FIGURE 2.13: Cumulative distribution functions of the histograms shown in Fig. 2.12 for BAL quasars from Schmidt et al. (1999) together with the Marin et al. (2014) AGN sample. The colour-coding and  $x$ -axis scale are the same as Fig. 2.12. The translucent vertical lines mark the median value in each sample.

references therein). This suggests a higher inclination (compared to non-BAL quasars) viewing angle for BALQSOs under the interpretation of a geometric model. Indeed, early polarisation studies explained the observations with a polar scattering region, viewed at an equatorial angle (e.g. [Goodrich & Miller 1995](#); [Cohen et al. 1995](#); [Lamy & Hutsemékers 2004](#)). Regardless of the true geometry, the reason for the difference must be understood. I would suggest that polarisation predictions are made from wind models such as the one I presented in chapter 5, using a similar approach to [Marin & Goosmann \(2013\)](#), but considering BALs in more detail. Overall, however, polarisation measurements seem to imply that BALQSOs are viewed from higher inclinations if geometric unification models are correct and are in slight tension with the idea that BAL quasars are viewed from the same range of angles as non-BAL quasars.

### 2.5.3 The Effect of Obscuration

[Caccianiga & Severgnini \(2011\)](#), hereafter C11) showed that the distribution of EW[O III] can also be well fitted by an obscuration model. They modelled the EW[O III] distribution using an absorption model based on column densities obtained from the *XMM* Newton Bright Serendipitous Source (XBS) sample. They use a sample size of 169 objects, and find that AGN with column densities of  $N_H \gtrsim 10^{22} \text{ cm}^{-2}$  can explain the high EW powerlaw tail.

The column density measurements for BAL quasars suggest that obscuration cannot explain the distribution of EW[O III] in quasars. As briefly discussed in chapter 5, BALs generally show strong X-ray absorption with column densities of  $N_H \gtrsim 10^{23} \text{ cm}^{-2}$  ([Green & Mathur 1996](#); [Mathur et al. 2000](#); [Green et al. 2001](#); [Grupe et al. 2003](#)). [Gallagher et al. \(1999\)](#) found all BAL quasars in a sample of 7 had  $N_H > 10^{22} \text{ cm}^{-2}$ , placing them firmly in the EW tail according to the C11 model. This is broadly consistent with the mean value of  $3.5 \times 10^{22} \text{ cm}^{-2}$  from [Morabito et al. \(2013\)](#), and would imply that BALQSOs should have significantly higher EWs if obscuration governs the EW[O III] distribution. Of course, only LoBAL quasars had EW[O III] measurements in the sample used here – this actually strengthens the conclusion, as low ionization BALQSOs show even higher column densities, approaching Compton-thick values ([Morabito et al. 2011](#)). This holds regardless of the outflow geometry adopted, so I suggest that the obscured model of C11 is ruled out on this basis.

### 2.5.4 Line Anisotropy

Optically thin lines are isotropic – the *local* escape probabilities in each direction are equal due to the low optical depth. When lines are optically thick, the situation is more complex, as local velocity gradients then determine the line anisotropy. Indeed, Keplerian velocity shear has been shown to modify the shape of disc-formed emission lines (Horne & Marsh 1986), and an additional radial shear from a wind can cause double-peaked lines to become single-peaked (Murray & Chiang 1996, 1997; Flohic et al. 2012).

R11 suggested that the broad emission lines trace the disc emission in terms of their anisotropy. If this was the case, we would not expect a difference in the BAL and non-BAL quasar EW distributions. However, an emission line would only be purely foreshortened if emitted by a disc with zero velocity shear. If the lines came from a region subject to Keplerian velocity shear then the surface brightness of an optically thick line is (Horne & Marsh 1986)

$$J_{\text{thick}}(\theta) \approx \cos \theta \ S_L \ \Delta\nu \ \sqrt{8 \ln \tau_0}, \quad (2.4)$$

where  $S_L$  is the line source function and  $\tau_0$  is the line centre optical depth, given by

$$\tau_0 = \frac{\mathcal{W}}{\sqrt{2\pi}\Delta\nu \cos \theta}. \quad (2.5)$$

The parameter  $\mathcal{W}$  is given by

$$\mathcal{W} = \frac{\pi e^2}{m_e c} f N', \quad (2.6)$$

where  $f$  is the oscillator strength and  $N'$  is the number density integrated along the vertical height of the disc. The linewidth  $\Delta\nu$  is enhanced from the thermal linewidth by the velocity shear, such that

$$\Delta\nu = \Delta\nu_{th} \left[ 1 + \left( \frac{3}{4} \frac{v_k}{v_{th}} \frac{H}{R} \right)^2 \sin^2 \theta \tan^2 \theta \sin^2 2\phi \right]^{1/2}. \quad (2.7)$$

Here,  $\phi$  is the azimuthal angle in the disc,  $v_{th}$  and  $v_{th}$  are the thermal line width in frequency and velocity units respectively,  $H$  is the scale height of the disc at radius  $R$ , and  $v_k$  is the Keplerian velocity.

The outcome of the Horne & Marsh (1986) analysis is that optically thick lines formed in a Keplerian disc are strongly anisotropic, but they do not follow a simple  $\cos \theta$  distribution. Instead, the angular emissivity function is a strong function of the velocity shear in the disc, the atomic physics of the line in question, the location of the line formation region and the vertical disc structure. It is hence possible that the broad emission lines are strongly anisotropic, and the presence of radial velocity shear from a wind would only complicate matters. I would therefore suggest that future efforts might include fully modelling the line emission as a function of inclination to feed into the above analysis.

Regardless of the precise angular distribution, line emission should not trace disc emission exactly, as we already know large-scale velocity fields are dynamically important in the BLR, purely from the line widths. In that case, one would expect systematic differences in EW between high inclination and low inclination sources, and these are not seen in the C IV 1550 Å and Mg II 2800 Å EW distributions.

## 2.6 Conclusions

I have explored the emission line properties of BAL and non-BAL quasars, particularly focusing on the EW distributions in two redshift ranges of the SDSS quasar catalog. My main conclusion is simply that the EW distributions of BAL and non-BAL quasars are remarkably similar, and this is not what one would expect from a unification model in which an equatorial BAL outflow rises from a foreshortened accretion disc. This geometry has been used extensively in geometric unification and BAL outflow models in the past (e.g. Murray et al. 1995; Proga et al. 2000; Proga & Kallman 2004; Risaliti & Elvis 2010; Borguet & Hutsemékers 2010; Higginbottom et al. 2013; Nomura et al. 2013, 2016), and was even adopted earlier in this thesis. I then established that an angular emissivity function of  $\epsilon(\theta) = \cos \theta$  is actually the conservative estimate from thin disc models, and used this to conduct a series of simulations similar to those conducted by Risaliti et al. (2011). As expected, these simulations confirmed the above finding.

Based on this analysis, it is possible to construct a few possible scenarios that favoured by the above results. These conclusions have the caveat that I have assumed that conclusions drawn about LoBAL quasars can be extended to BAL quasars in general.

- *Scenario 1:* The quasar continuum is much more isotropic than one would expect from a geometrically thin, optically thick accretion disc. I have demonstrated that general relativistic effects cannot account for this discrepancy in the UV. Reprocessing by surrounding dense plasma with a large covering factor or limb brightening in the disc may provide possible explanations which this analysis cannot yet confirm or refute.
- *Scenario 2:* Quasar discs are strongly anisotropic, as expected from a geometrically thin, optically thick accretion disc. In this case, BAL outflows cannot only emerge at extreme inclinations and should instead be seen at very similar angles to non-BAL quasars. Polarisation measurements need to be reconciled with this hypothesis. I recommend that future RT modelling efforts explore different outflow geometries and that detailed polarisation modelling is undertaken to constrain the outflow opening angles.
- *Scenario 3:* The geometric unification model does not explain the incidence of BALs in quasars, or requires an additional component which is *time-dependent*, such as an evolutionary or accretion state origin for BAL outflows. In this scenario, BAL quasars would be seen from very similar angles to non-BAL quasars. If this is the case, the covering factors and opening angles of the outflows still need to be constrained so that feedback efficiencies can be accurately estimated.

I have confirmed that obscuration cannot explain the EW distributions of all quasars due to the high column density observed in BAL (and particularly LoBAL) quasars. It is possible that line opacity could explain the observed similarities between the broad emission line distributions, but this cannot explain the similarities in the LoBAL and non-BAL quasar EW[O III] distributions, as O III is a forbidden, optically thin transition.

Regardless of the conclusions about BAL quasars and their outflow geometries, this analysis allows conclusions to be drawn about the *overall* quasar population. In scenario 1, the EW[O III] distribution of quasars cannot be driven by inclination as suggested by (Risaliti et al. 2011). This would imply that EW[O III] is a poor orientation indicator. The lack of correlation between EW[O III] and FWHM[H $\beta$ ] also suggests that it is not possible for them both to be strongly orientation dependent. Even if scenario 1 holds, then FWHM[H $\beta$ ] and EV1 measurements of LoBALs imply that they are seen from similar inclinations to type 1 quasars.

The above three scenarios each pose a different challenge to the current understanding of, respectively, accretion physics, outflow models and our understanding of unification and the BAL fraction. This work therefore adds to the growing evidence that our simplest models are not sufficient to describe the overall quasars and that alternatives should be sought.



# Bibliography

- Alexander D. M., Bauer F. E., Brandt W. N., Daddi E. et al., 2011, ApJ 738, 44
- Allen J. T., Hewett P. C., Maddox N., Richards G. T., Belokurov V., 2011, MNRAS 410, 860
- Antonucci R., 1988, in M. Kafatos (ed.), Supermassive Black Holes, p. 26
- Antonucci R., 2013, Nature 495, 165
- Antonucci R., Geller R., Goodrich R. W., Miller J. S., 1996, ApJ 472, 502
- Antonucci R. R. J., Miller J. S., 1985, ApJ 297, 621
- Arévalo P., Uttley P., 2006, MNRAS 367, 801
- Balbus S. A., Hawley J. F., 1991, ApJ 376, 214
- Baldi R. D., Capetti A., Robinson A., Laor A., Behar E., 2016, MNRAS
- Bartlett E., 2013, Ph.D. thesis, University of Southampton
- Baskin A., Laor A., 2005, MNRAS 358, 1043
- Belloni T. (ed.), 2010, The Jet Paradigm, Vol. 794 of *Lecture Notes in Physics, Berlin Springer Verlag*
- Benz A. O., Fuerst E., Kiplinger A. L., 1983, Nature 302, 45
- Blandford R. D., Payne D. G., 1982, MNRAS 199, 883
- Blandford R. D., Znajek R. L., 1977, MNRAS 179, 433
- Bondi H., 1952, MNRAS 112, 195
- Bondi H., Hoyle F., 1944, MNRAS 104, 273
- Bonning E. W., Cheng L., Shields G. A., Salviander S., Gebhardt K., 2007, ApJ 659, 211
- Borguet B., Hutsemékers D., 2010, A&A 515, A22
- Borguet B. C. J., Edmonds D., Arav N., Dunn J., Kriss G. A., 2012, ApJ 751, 107
- Boroson T. A., Green R. F., 1992, ApJs 80, 109
- Brotherton M. S., De Breuck C., Schaefer J. J., 2006, MNRAS 372, L58
- Caccianiga A., Severgnini P., 2011, MNRAS 415, 1928

- Capellupo D. M., Netzer H., Lira P., Trakhtenbrot B., Mejía-Restrepo J., 2015, MNRAS 446, 3427
- Cassinelli J. P., 1979, ARAA 17, 275
- Chartas G., Kochanek C. S., Dai X., Poindexter S., Garmire G., 2009, ApJ 693, 174
- Cohen M. H., Ogle P. M., Tran H. D., Vermeulen R. C. et al., 1995, ApJ Letters 448, L77
- Cohen R. D., Puetter R. C., Rudy R. J., Ake T. B., Foltz C. B., 1986, ApJ 311, 135
- Connolly S. D., McHardy I. M., Dwelly T., 2014, MNRAS 440, 3503
- Connolly S. D., McHardy I. M., Skipper C. J., Emmanoulopoulos D., 2016, MNRAS
- Coppejans D. L., Körding E. G., Miller-Jones J. C. A., Rupen M. P. et al., 2015, MNRAS 451, 3801
- Cordova F. A., Mason K. O., 1982, ApJ 260, 716
- Crenshaw D. M., Rodriguez-Pascual P. M., Penton S. V., Edelson R. A. et al., 1996, ApJ 470, 322
- Crummy J., Fabian A. C., Gallo L., Ross R. R., 2006, MNRAS 365, 1067
- Dabrowski Y., Fabian A. C., Iwasawa K., Lasenby A. N., Reynolds C. S., 1997, MNRAS 288, L11
- Dai X., Kochanek C. S., Chartas G., Kozłowski S. et al., 2010, ApJ 709, 278
- Dai X., Shankar F., Sivakoff G. R., 2012, ApJ 757, 180
- Davis S. W., Hubeny I., 2006, ApJs 164, 530
- Davis S. W., Woo J.-H., Blaes O. M., 2007, ApJ 668, 682
- Denney K. D., De Rosa G., Croxall K., Gupta A. et al., 2014, ApJ 796, 134
- Dexter J., Agol E., 2011, ApJ Letters 727, L24
- Dhillon V. S., 1996, in A. Evans, J. H. Wood (eds.), IAU Colloq. 158: Cataclysmic Variables and Related Objects, Vol. 208 of *Astrophysics and Space Science Library*, 3
- Dhillon V. S., Rutten R. G. M., 1995, MNRAS 277, 777
- Díaz Trigo M., Boirin L., 2015, ArXiv e-prints
- DiPompeo M. A., Brotherton M. S., Cales S. L., Runnoe J. C., 2012a, MNRAS 427, 1135
- DiPompeo M. A., Brotherton M. S., De Breuck C., 2012b, ApJ 752, 6
- Done C., Davis S. W., Jin C., Blaes O., Ward M., 2012, MNRAS 420, 1848
- Done C., Jin C., 2015, ArXiv e-prints
- Echevarria J., 1988, MNRAS 233, 513

- Edelson R., Gelbord J. M., Horne K., McHardy I. M. et al., 2015, ApJ 806, 129
- Edge D. O., Shakeshaft J. R., McAdam W. B., Baldwin J. E., Archer S., 1959, MmRA 68, 37
- Eggleton P. P., 1983, ApJ 268, 368
- Ehman J. R., Dixon R. S., Kraus J. D., 1970, AJ 75, 351
- Ekers J. A., 1969, Australian Journal of Physics Astrophysical Supplement 7
- Elitzur M., 2012, ApJ Letters 747, L33
- Elitzur M., Ho L. C., Trump J. R., 2014, MNRAS 438, 3340
- Elvis M., 2000, ApJ 545, 63
- Elvis M., Wilkes B. J., McDowell J. C., Green R. F. et al., 1994, ApJs 95, 1
- Emmanoulopoulos D., Papadakis I. E., Dovčiak M., McHardy I. M., 2014, MNRAS 439, 3931
- Emmanoulopoulos D., Papadakis I. E., McHardy I. M., Arévalo P. et al., 2012, MNRAS 424, 1327
- Evans P. A., Hellier C., Ramsay G., Cropper M., 2004, MNRAS 349, 715
- Fabian A. C., 2012, ARAA 50, 455
- Fabian A. C., Nandra K., Reynolds C. S., Brandt W. N. et al., 1995, MNRAS 277, L11
- Fath E. A., 1909, Lick Observatory Bulletin 5, 71
- Fender R. P., 2001, MNRAS 322, 31
- Fender R. P., Belloni T. M., Gallo E., 2004, MNRAS 355, 1105
- Fender R. P., Gallo E., Russell D., 2010, MNRAS 406, 1425
- Flohic H. M. L. G., Eracleous M., Bogdanović T., 2012, ApJ 753, 133
- Frank J., King A., Raine D., 1992, Accretion power in astrophysics.
- Gallagher S. C., Brandt W. N., Sambruna R. M., Mathur S., Yamasaki N., 1999, ApJ 519, 549
- Gallo E., Fender R. P., Pooley G. G., 2003, MNRAS 344, 60
- Gandhi P., Höning S. F., Kishimoto M., 2015, ApJ 812, 113
- Gandhi P., Terashima Y., Yamada S., Mushotzky R. F. et al., 2013, ApJ 773, 51
- Gardner E., Done C., 2016, ArXiv e-prints
- Gierliński M., Done C., 2004, MNRAS 349, L7
- Gierliński M., Done C., 2006, MNRAS 371, L16
- Goodrich R. W., Miller J. S., 1995, ApJ Letters 448, L73
- Green A. R., McHardy I. M., Lehto H. J., 1993, MNRAS 265, 664
- Green P. J., Aldcroft T. L., Mathur S., Wilkes B. J., Elvis M., 2001, ApJ 558, 109

- Green P. J., Mathur S., 1996, ApJ 462, 637
- Greenstein J. L., Oke J. B., 1982, ApJ 258, 209
- Grupe D., Mathur S., Elvis M., 2003, AJ 126, 1159
- Gu M., Cao X., 2009, MNRAS 399, 349
- Hōshi R., 1979, Progress of Theoretical Physics 61, 1307
- Haardt F., Maraschi L., 1991, ApJ Letters 380, L51
- Häring N., Rix H.-W., 2004, ApJ Letters 604, L89
- Hassall B. J. M., 1985, MNRAS 216, 335
- Haug K., 1987, AP&SS 130, 91
- Hazard C., Mackey M. B., Shimmins A. J., 1963, Nature 197, 1037
- Heap S. R., Boggess A., Holm A., Klinglesmith D. A. et al., 1978, Nature 275, 385
- Heil L. M., Vaughan S., Uttley P., 2012, MNRAS 422, 2620
- Hessman F. V., Robinson E. L., Nather R. E., Zhang E.-H., 1984, ApJ 286, 747
- Higginbottom N., Knigge C., Long K. S., Sim S. A., Matthews J. H., 2013, MNRAS 436, 1390
- Hoare M. G., Drew J. E., 1991, MNRAS 249, 452
- Hoare M. G., Drew J. E., 1993, MNRAS 260, 647
- Hogg J. D., Reynolds C., 2015, ArXiv e-prints
- Honeycutt R. K., Schlegel E. M., Kaitchuck R. H., 1986, ApJ 302, 388
- Hönig S. F., Kishimoto M., Tristram K. R. W., Prieto M. A. et al., 2013, ApJ 771, 87
- Horne K., 1993, Eclipse Mapping of Accretion Disks: The First Decade, 117
- Horne K., Marsh T. R., 1986, MNRAS 218, 761
- Hoyle F., Lyttleton R. A., 1939, Proceedings of the Cambridge Philosophical Society 35, 405
- Hubeny I., Agol E., Blaes O., Krolik J. H., 2000, ApJ 533, 710
- Idan I., Lasota J.-P., Hameury J.-M., Shaviv G., 2010, A&A 519, A117
- Iwasawa K., Fabian A. C., Mushotzky R. F., Brandt W. N. et al., 1996a, MNRAS 279, 837
- Iwasawa K., Fabian A. C., Reynolds C. S., Nandra K. et al., 1996b, MNRAS 282, 1038
- Janiuk A., Czerny B., Madejski G. M., 2001, ApJ 557, 408
- Ju W., Stone J. M., Zhu Z., 2016, ArXiv e-prints
- Kafka S., Honeycutt R. K., 2004, AJ 128, 2420
- King A., 2003, ApJ Letters 596, L27
- Knigge C., 1999, MNRAS 309, 409

- Knigge C., Baraffe I., Patterson J., 2011, ApJs 194, 28
- Knigge C., Long K. S., Wade R. A., Baptista R. et al., 1998a, ApJ 499, 414
- Knigge C., Long K. S., Wade R. A., Baptista R. et al., 1998b, ApJ 499, 414
- Knigge C., Scaringi S., Goad M. R., Cottis C. E., 2008, MNRAS 386, 1426
- Koratkar A., Blaes O., 1999, PASP 111, 1
- Körding E., Rupen M., Knigge C., Fender R. et al., 2008, Science 320, 1318
- Körding E. G., Jester S., Fender R., 2006, MNRAS 372, 1366
- Kotov O., Churazov E., Gilfanov M., 2001, MNRAS 327, 799
- Kraft R. P., Mathews J., Greenstein J. L., 1962, ApJ 136, 312
- Krolik J. H., Begelman M. C., 1986, in Bulletin of the American Astronomical Society, Vol. 18 of *BAAS*, 903
- Krolik J. H., Voit G. M., 1998, ApJ Letters 497, L5
- Kuulkers E., Motta S., Kajava J., Homan J. et al., 2015, The Astronomer's Telegram 7647
- La Dous C., 1989, MNRAS 238, 935
- Lamy H., Hutsemékers D., 2004, A&A 427, 107
- Laor A., 1991, ApJ 376, 90
- Laor A., Davis S. W., 2014, MNRAS 438, 3024
- Lasota J.-P., 2001, NAR 45, 449
- Lazarova M. S., Canalizo G., Lacy M., Sajina A., 2012, ApJ 755, 29
- Liebert J., Stockman H. S., 1985, in D. Q. Lamb, J. Patterson (eds.), *Cataclysmic Variables and Low-Mass X-ray Binaries*, Vol. 113 of *Astrophysics and Space Science Library*, p. 151
- Long K. S., Blair W. P., Davidsen A. F., Bowers C. W. et al., 1991, ApJ Letters 381, L25
- Long K. S., Knigge C., 2002, ApJ 579, 725
- Long K. S., Wade R. A., Blair W. P., Davidsen A. F., Hubeny I., 1994, ApJ 426, 704
- Lusso E., Worseck G., Hennawi J. F., Prochaska J. X. et al., 2015, MNRAS 449, 4204
- Lynden-Bell D., 1969, Nature 223, 690
- Lyubarskii Y. E., 1997, MNRAS 292, 679
- Madau P., Ghisellini G., Fabian A. C., 1994, MNRAS 270, L17
- Magdziarz P., Blaes O. M., Zdziarski A. A., Johnson W. N., Smith D. A., 1998, MNRAS 301, 179
- Magorrian J., Tremaine S., Richstone D., Bender R. et al., 1998, AJ 115, 2285

- Mangham S. W., Knigge C., Matthews J. H., Long K. S. et al., 2016, in prep.
- Marin F., 2014, MNRAS 441, 551
- Marin F., 2016, ArXiv e-prints
- Marin F., Goosmann R. W., 2013, MNRAS 436, 2522
- Marinucci A., Bianchi S., Matt G., Alexander D. M. et al., 2016, MNRAS 456, L94
- Marscher A. P., 2006, in P. A. Hughes, J. N. Bregman (eds.), Relativistic Jets: The Common Physics of AGN, Microquasars, and Gamma-Ray Bursts, Vol. 856 of *American Institute of Physics Conference Series*, p. 1
- Marsh T. R., Horne K., 1990, ApJ 349, 593
- Marziani P., Sulentic J. W., Zwitter T., Dultzin-Hacyan D., Calvani M., 2001, ApJ 558, 553
- Mathur S., Green P. J., Arav N., Brotherton M. et al., 2000, ApJ Letters 533, L79
- Matt G., Guainazzi M., Maiolino R., 2003, MNRAS 342, 422
- Mauche C. W., 1996, ArXiv Astrophysics e-prints
- McHardy I. M., Koerding E., Knigge C., Uttley P., Fender R. P., 2006, Nature 444, 730
- McHardy I. M., Papadakis I. E., Uttley P., 1999, Nuclear Physics B Proceedings Supplements 69, 509
- Merloni A., Heinz S., di Matteo T., 2003, MNRAS 345, 1057
- Meyer F., Meyer-Hofmeister E., 1981, A&A 104, L10
- Mihalas D., 1978, Stellar atmospheres /2nd edition/
- Miller L., Turner T. J., 2013, ApJ Letters 773, L5
- Miller L., Turner T. J., Reeves J. N., 2008, A&A 483, 437
- Misra R., Kembhavi A. K., 1998, ApJ 499, 205
- Mitsuda K., Inoue H., Nakamura N., Tanaka Y., 1989, PASJ 41, 97
- Morabito L. K., Dai X., Leighly K. M., Sivakoff G. R., Shankar F., 2011, ApJ 737, 46
- Morabito L. K., Dai X., Leighly K. M., Sivakoff G. R., Shankar F., 2013, ArXiv e-prints
- Morgan C. W., Kochanek C. S., Morgan N. D., Falco E. E., 2010, ApJ 712, 1129
- Motta S., Beardmore A., Oates S., Sanna N. P. M. K. A. et al., 2015, The Astronomer's Telegram 7665
- Muñoz-Darias T., Coriat M., Plant D. S., Ponti G. et al., 2013, MNRAS 432, 1330
- Murray N., Chiang J., 1996, Nature 382, 789
- Murray N., Chiang J., 1997, ApJ 474, 91
- Murray N., Chiang J., Grossman S. A., Voit G. M., 1995, ApJ 451, 498
- Nandra K., Pounds K. A., 1994, MNRAS 268, 405

- Narayan R., McClintock J. E., 2012, MNRAS 419, L69
- Narayan R., McClintock J. E., Tchekhovskoy A., 2014, Energy Extraction from Spinning Black Holes Via Relativistic Jets, 523
- Narayan R., Yi I., 1994, ApJ Letters 428, L13
- Narayan R., Yi I., 1995, ApJ 452, 710
- Neugebauer G., Oke J. B., Becklin E. E., Matthews K., 1979, ApJ 230, 79
- Noebauer U. M., Long K. S., Sim S. A., Knigge C., 2010, ApJ 719, 1932
- Nomura M., Ohsuga K., Takahashi H. R., Wada K., Yoshida T., 2016, PASJ 68, 16
- Nomura M., Ohsuga K., Wada K., Susa H., Misawa T., 2013, PASJ 65, 40
- Osaki Y., 1974, PASJ 26, 429
- Patterson J., 1984, ApJs 54, 443
- Patterson J., 1994, PASP 106, 209
- Patterson J., Patino R., Thorstensen J. R., Harvey D. et al., 1996, AJ 111, 2422
- Penrose R., Floyd R. M., 1971, Nature Physical Science 229, 177
- Perley R. A., Dreher J. W., Cowan J. J., 1984, ApJ Letters 285, L35
- Ponti G., Fender R. P., Begelman M. C., Dunn R. J. H. et al., 2012, MNRAS 422, L11
- Potash R. I., Wardle J. F. C., 1980, ApJ 239, 42
- Pounds K. A., Nandra K., Stewart G. C., Leighly K., 1989, MNRAS 240, 769
- Pounds K. A., Reeves J. N., 2009, MNRAS 397, 249
- Pringle J. E., 1981, ARAA 19, 137
- Proga D., 2005, in J.-M. Hameury, J.-P. Lasota (eds.), *The Astrophysics of Cataclysmic Variables and Related Objects*, Vol. 330 of *Astronomical Society of the Pacific Conference Series*, 103
- Proga D., Kallman T. R., 2004, ApJ 616, 688
- Proga D., Stone J. M., Kallman T. R., 2000, ApJ 543, 686
- Puccetti S., Fiore F., Risaliti G., Capalbi M. et al., 2007, MNRAS 377, 607
- Reeves J. N., O'Brien P. T., Ward M. J., 2003, ApJ Letters 593, L65
- Reynolds C. S., 1999, in J. Poutanen, R. Svensson (eds.), *High Energy Processes in Accreting Black Holes*, Vol. 161 of *Astronomical Society of the Pacific Conference Series*, 178
- Ringwald F. A., Naylor T., 1998, AJ 115, 286
- Risaliti G., Elvis M., 2010, A&A 516, A89
- Risaliti G., Elvis M., Fabbiano G., Baldi A. et al., 2007, ApJ Letters 659, L111
- Risaliti G., Elvis M., Nicastro F., 2002, ApJ 571, 234

- Risaliti G., Salvati M., Marconi A., 2011, MNRAS 411, 2223
- Ross R. R., Fabian A. C., 2005, MNRAS 358, 211
- Rottenberg J. A., 1952, MNRAS 112, 125
- Rutten R. G. M., van Paradijs J., Timmerman J., 1992, A&A 260, 213
- Scaringi S., Körding E., Uttley P., Knigge C. et al., 2012, MNRAS 421, 2854
- Scaringi S., Maccarone T. J., Koerding E., Knigge C. et al., 2015, ArXiv e-prints
- Schmidt G. D., Hines D. C., 1999, ApJ 512, 125
- Schmidt M., 1963, Nature 197, 1040
- Schmidt M., 1965a, ApJ 141, 1295
- Schmidt M., 1965b, ApJ 141, 1
- Setti G., Woltjer L., 1989, A&A 224, L21
- Seyfert C. K., 1943, ApJ 97, 28
- Shakura N. I., Sunyaev R. A., 1973, A&A 24, 337
- Shankar F., Calderone G., Knigge C., Matthews J. et al., 2016, ApJ Letters 818, L1
- Shaviv G., Wehrse R., 1991, A&A 251, 117
- Shen Y., Ho L. C., 2014, Nature 513, 210
- Shen Y., Richards G. T., Strauss M. A., Hall P. B. et al., 2011, ApJs 194, 45
- Shi Y., Rieke G. H., Smith P., Rigby J. et al., 2010, ApJ 714, 115
- Silk J., Rees M. J., 1998, A&A 331, L1
- Sim S. A., Drew J. E., Long K. S., 2005, MNRAS 363, 615
- Sim S. A., Miller L., Long K. S., Turner T. J., Reeves J. N., 2010, MNRAS 404, 1369
- Smak J., 1981, ACTAA 31, 395
- Sobolewska M. A., Siemiginowska A., Gierliński M., 2011, MNRAS 413, 2259
- Springel V., Di Matteo T., Hernquist L., 2005, ApJ Letters 620, L79
- Spruit H. C., 1996, in R. A. M. J. Wijers, M. B. Davies, C. A. Tout (eds.), NATO Advanced Science Institutes (ASI) Series C, Vol. 477 of *NATO Advanced Science Institutes (ASI) Series C*, p. 249
- Stockman H. S., Angel J. R. P., Miley G. K., 1979, ApJ Letters 227, L55
- Struve O., 1935, ApJ 81, 66
- Suleimanov V., Hertfelder M., Werner K., Kley W., 2014, ArXiv e-prints
- Sulentic J. W., Zwicky T., Marziani P., Dultzin-Hacyan D., 2000, ApJ Letters 536, L5
- Thorne K. S., 1974, ApJ 191, 507
- Tohline J. E., Osterbrock D. E., 1976, ApJ Letters 210, L117
- Tombesi F., Cappi M., Reeves J. N., Palumbo G. G. C. et al., 2010, A&A 521, A57

- Tran H. D., 2001, ApJ Letters 554, L19
- Urrutia T., Becker R. H., White R. L., Glikman E. et al., 2009, ApJ 698, 1095
- Urry C. M., Padovani P., 1995, PASP 107, 803
- Uttley P., Cackett E. M., Fabian A. C., Kara E., Wilkins D. R., 2014, AAPR 22, 72
- Uttley P., McHardy I. M., 2001, MNRAS 323, L26
- Uttley P., McHardy I. M., Vaughan S., 2005, MNRAS 359, 345
- Van de Sande M., Scaringi S., Knigge C., 2015, MNRAS 448, 2430
- Vestergaard M., Wilkes B. J., 2001, ApJs 134, 1
- Wade R. A., 1984, MNRAS 208, 381
- Wade R. A., 1988, ApJ 335, 394
- Wang B., Han Z., 2012, NAR 56, 122
- Warner B., 2003, Cataclysmic Variable Stars
- Weymann R. J., Morris S. L., Foltz C. B., Hewett P. C., 1991, ApJ 373, 23
- White N. E., Stella L., Parmar A. N., 1988, ApJ 324, 363
- Woltjer L., 1959, ApJ 130, 38
- Zakamska N. L., Strauss M. A., Krolik J. H., Collinge M. J. et al., 2003, AJ 126, 2125
- Zanstra H., 1929, Publications of the Dominion Astrophysical Observatory Victoria 4, 209
- Zhang S. N., Cui W., Chen W., 1997, ApJ Letters 482, L155
- Zhou H., Wang T., Wang H., Wang J. et al., 2006, ApJ 639, 716